Nanoscale Advances

ROYAL SOCIETY OF CHEMISTRY

MINIREVIEW

View Article Online
View Journal | View Issue

Cite this: *Nanoscale Adv.*, 2021, **3**, 867

Hybrid magnetic nanoparticles as efficient nanoheaters in biomedical applications

Gabriel C. Lavorato, *[a] Raja Das,[bc] Javier Alonso Masa,[d] Manh-Huong Phan[e] and Hariharan Srikanth *[e]

Heating at the nanoscale is the basis of several biomedical applications, including magnetic hyperthermia therapies and heat-triggered drug delivery. The combination of multiple inorganic materials in hybrid magnetic nanoparticles provides versatile platforms to achieve an efficient heat delivery upon different external stimuli or to get an optical feedback during the process. However, the successful design and application of these nanomaterials usually require intricate synthesis routes and their magnetic response is still not fully understood. In this review we give an overview of the novel systems reported in the last few years, which have been mostly obtained by organic phase-based synthesis and epitaxial growth processes. Since the heating efficiency of hybrid magnetic nanoparticles often relies on the exchange-interaction between their components, we discuss various interface-phenomena that are responsible for their magnetic properties. Finally, followed by a brief comment on future directions in the field, we outline recent advances on multifunctional nanoparticles that can boost the heating power with light and combine heating and temperature sensing in a single nanomaterial.

Received 6th October 2020
Accepted 6th January 2021

DOI: 10.1039/d0na00828a

rsc.li/nanoscale-advances

[a]*Instituto de Investigaciones Fisicoquímicas Teóricas y Aplicadas (INIFTA-CONICET), Universidad Nacional de La Plata, 1900 La Plata, Argentina. E-mail: gclavorato@inifta.unlp.edu.ar*

[b]*Faculty of Materials Science and Engineering and Phenikaa Institute for Advanced Study (PIAS), Phenikaa University, Hanoi, 10000, Vietnam*

[c]*Phenikaa Research and Technology Institute (PRATI), A&A Green Phoenix Group, 167 Hoang Ngan, Hanoi 10000, Vietnam*

[d]*Departamento CITIMAC, Universidad de Cantabria, Santander 39005, Spain*

[e]*Department of Physics, University of South Florida, 33620 Tampa, FL, USA. E-mail: sharihar@usf.edu*

1. Introduction

The optimization of the heating efficiency of magnetic nanoparticles (MNPs) can shape their future in biomedical applications, such as hyperthermia therapy,[1,2] heat-mediated drug delivery,[3,4] and heat-triggered control of biological processes.[5,6] At the same time, local heating phenomena have been demonstrated to be also important in other scientific areas, such as catalysis[7] and self-healing polymers.[8]

Gabriel Lavorato obtained his Engineering Sciences PhD degree in 2016 at the Balseiro Institute, National University of Cuyo, Argentina. Following a post-doctoral position at the Brazilian Center for Research in Physics and a Fulbright Visiting Scientist Scholarship at the University of South Florida, in 2018 he joined the National Scientific and Technical Research Council and National University of La Plata, Argentina, as Assistant Researcher. He is currently part of the NanoBioMed Group at INIFTA, and his research interests include the physical chemistry of metal oxide nanostructures and their technological applications.

Raja Das received his PhD in Chemical Sciences from CSIR-National Chemical Laboratory, India in 2014. He was a post-doctoral fellow at University of South Florida, USA and National Institute for Materials Science, Japan from 2014 to 2018. He is now an Assistant Professor in the Faculty of Materials Science and Engineering, Phenikaa University, Hanoi, Vietnam. He is leader of the research group, Nanomaterials for Electronics and Renewable Energy Laboratory. His research group focuses on the design, synthesis and applications of advanced nanomaterials for thermoelectric, spintronic and biomedical applications, including magnetic hyperthermia therapy and drug delivery.

The current knowledge on chemistry and magnetism at the nanoscale has enabled the design of a large number of nanostructures with controlled physical and chemical properties, as a result of a fine tuning of their size, shape and composition.[9] However, to overcome intrinsic limitations of these single-phase systems, two (or more) inorganic materials can be combined to form hybrid nanoparticles (HNPs). The most widespread synthesis route is based on the epitaxial growth of the individual components in a seed-mediated process, which has triggered basic studies since novel properties are emerging as a result of a profound understanding and control of the interface characteristics.[10–12] The integration of different magnetic components can improve the heating efficiency through an additional degree of freedom to tune the magnetic anisotropy provided by the interface exchange coupling.[13] In addition, it has been shown that magnetically and optically responsive components can be combined in HNPs, resulting in an enhanced heating power[2,14] and enabling an appropriate multifunctional platform to provide feedback on the local temperature at the NP surroundings.[15,16]

There has been a number of good review papers on the properties and biomedical applications of MNPs in the literature.[17–26] Some have dealt with the designs of novel MNP architectures to optimize their heating ability[17–19] or have devoted to multimodal heating[20,21] and local temperature sensing,[22] but have not focused on HNPs. The others[23,25,26] have provided a general overview of HNPs that also included non-magnetic, polymeric or semiconducting materials, but with marginal discussions on their heating ability. Here, we provide insights into recent reports on inorganic HNPs with at least one magnetic component. We assess recent advances in the synthesis routes and outline the remarkable magnetic properties reported in the last few years, as well as the mechanisms behind the control of their heating efficiency.

Since most of the reported systems rely on multi-step organic-phase synthesis routes, in Section 2 we briefly introduce their fundamental aspects. To this end, we highlight the important findings on HNPs obtained by solution-based epitaxial growth, cation-exchange and surface passivation routes. Next, in Section 3 we review the basic notions of magnetism at the nanoscale that lay the main concepts of magnetic inductive heating, including the theoretical and modelling approaches. Since the magnetic properties of HNPs are closely related to the physics at the interface, Section 4 provides deeper insights, through a careful review of recent publications, into the interface-mediated magnetic phenomena and their relations to the heating efficiency. This section consists of four different aspects: (i) interface exchange-coupling, (ii) imperfect coupling through defective-nanoparticles, (iii) ultrathin shells, and (iv) modelling of the heating power in HNPs. The important role the HNPs play is analyzed and discussed in terms of their magnetic and heating responses, which are governed by the nanostructure design. While Section 4 mostly focuses on HNPs defined by their

Javier defended his PhD in 2010 on Collective Magnetic Behaviors in Granular Thin Films, and afterwards, he was working as a Post-doctoral Researcher at the University of South Florida (USA), where he started a new research line on Anisotropic Magnetic Nanostructures for Magnetic Hyperthermia of Cancer Treatment. Since 2018, he has been working as Assistant Professor at the University of Cantabria where he is leading a project on Remotely Controlled Magnetotactic Bacteria for Biomedical Applications.

Manh-Huong Phan is Professor of Physics at the University of South Florida. He received a Ph.D. degree in Engineering Physics from Bristol University in 2006. His research interests lie in the physics and applications of nanomagnetism and nanomaterials, with an expertise on the development of novel materials exhibiting magneto-caloric and magnetoimpedance effects for energy-efficient magnetic refrigeration and smart sensor technologies. Recently, his group has discovered the room temperature ferromagnetism and new phenomena in atomically thin van der Waals magnets that could revolutionize spintronics, valleytronics, and quantum information science. He has published nearly 290 peer-reviewed journal papers and 1 textbook.

Hari Srikanth is a Distinguished University Professor in the Physics Department at University of South Florida. He directs the Functional Materials Laboratory and his research focus areas are advanced magnetic materials, applications of magnetic nanoparticles in nanomedicine and RF devices, magnetic refrigeration, spin caloric phenomena and complex oxides. He has over 275 journal publications and has given over 200 invited talks. Hari is a Fellow of the American Physical Society and a Senior Member of IEEE. He served as an IEEE Magnetics Society Distinguished Lecturer in 2019. He is currently an Editor for Journal of Alloys and Compounds.

intraparticle interactions, Section 5 is devoted to multifunctional HNPs. Recent works regarding the integration of heating and temperature sensing in a single nanostructure and the improvement of the heating power with optical excitation are reviewed. Finally, an overview of the application of HNPs to magnetic hyperthermia therapies and beyond is given in Section 6.

The development of HNPs for heat-mediated biomedical applications is a rapidly advancing field that requires an interdisciplinary approach in the crossover of materials science, physics, chemistry and biology. The main goal of this article is to provide a review of the latest advances on the optimization of their heating ability through three interrelated concepts: (i) the epitaxial growth and chemical stability of nanostructures, (ii) the interface-mediated effects on the magnetic properties, and (iii) the expanded multifunctionalities by the combination of different stimuli-responsive materials.

2. Synthesis routes and novel hybrid systems

The synthesis of HNPs has evolved significantly in the last decades, and several methods have been reported, including physical and chemical routes in either aqueous or organic solvents.[9,27] Since most of the novel HNPs for efficient heating at the nanoscale have been produced by organic-phase routes, we will start by introducing some of its basic principles. Reactions in organic solutions involve the thermal decomposition of organometallic compounds in high boiling temperature solvents (200–350 °C) and allow for the stabilization of the nanocrystals by a library of different surfactants, mostly long-chain acids, amines or phosphines according to the required chemical binding.[9] This scheme enables an outstanding control of the composition, size, polydispersity and shape of the NP components,[9] which is essentially achieved through a nucleation step (based on the rapid monomer supersaturation promoted by hot injection or heat-up methods) well-separated from a diffusion-limited growth stage.[28]

Most approaches to the synthesis of HNPs are based on a seed-mediated process where the seeds are previously prepared and mixed with the precursors to form the second inorganic component, a strategy that resembles the seed-mediated routes developed for semiconductor HNPs[29] and for the precise size control of single-phase MNPs.[30] Notably, both epitaxial[31,32] and non-epitaxial[33] approaches have been reported. In an epitaxial growth, the synthesis of the second component is driven by the exposed facets of the seeds and a heterogeneous nucleation enables the formation of the second phase by stabilizing nuclei on the seeds' surface.[32] The thermodynamic parameters of homogeneous and heterogeneous nucleation can be very different and depend strongly on the interface energy between the seed and the nuclei (E_γ). When E_γ is sufficiently low, the energy barrier for heterogeneous nucleation is low and the seed will be fully covered by the shell phase to form a core/shell structure. Such a low E_γ is accomplished, for example, if both components have similar crystal structures and a small lattice mismatch. On the other hand, if E_γ is large, a high energy barrier can block the heterogeneous nucleation and the nuclei may not be able to grow over the whole seed surface, leading to asymmetric nanostructures with anisotropic morphologies, such as Janus HNPs.[32,34,35] It is worth mentioning that, apart from the lattice structure, the chemical affinity between both materials can also promote a heterogeneous nucleation,[32] which has been proposed to synthesize non-epitaxial HNPs[33] in a more complex framework that could allow for a greater variety of possible materials.

In this section, we will review the solution-based synthesis routes that have recently been employed to obtain HNPs. We will integrate different perspectives by including epitaxial growth- and cation exchange-based routes, as well as surface passivation and recent advances in combining plasmonic materials and iron oxides.

2a Epitaxial hybrid nanostructures

Heteroepitaxy can offer an unprecedented control of the physicochemical properties in colloidal nano-synthesis by applying several concepts from thin films research.[10,36] In an epitaxial growth, a material with a well-defined crystal orientation with respect to a crystalline substrate is obtained. This concept has recently been proposed to design HNPs with an outstanding control of grain-boundaries in multigrain shells.[10,37] For example, a precisely oriented tetragonal phase (Mn_3O_4) can be grown on the {100} facets of a spinel phase (*e.g.* Co_3O_4 nanocubes, although other materials can also be used[10]), as summarized in Fig. 1A. Such approach enables the development of specific grain boundaries between the shell grains, whose lattice is distorted near the edges of the cubes. This tight control of grain boundaries in HNPs might offer novel, still unexplored, tools to tune their magnetic properties through nanointerface chemistry.[38] In another example, Pratt *et al.*[12] studied oxidized metal Fe nanocubes and demonstrated that the multigrain iron oxide lattice at the surface is strained because of the mismatch between the oxide and the metal lattices. Strain gradients are formed due to the cubic morphology of the nanoparticles, leading to an enhanced diffusion of cations and an oxidation process that is ultimately determined by the crystal strain in the oxide shell. Since the oxidation extent of iron-based nanostructures can determine their heating efficiency,[39,40] novel ways to control the underlying mechanisms are highly relevant.

As mentioned above, the simplest way to synthesize epitaxial HNPs is to grow a second component with a similar crystal structure and a low lattice mismatch through a seed-mediated approach. Spinel ferrites are excellent candidates to this end, thanks to the rich variety of phases with similar crystal lattices and composition-driven different chemical and magnetic properties.[41] Therefore, numerous epitaxial core/shell HNPs have been produced with an excellent control over their magnetic properties by combining Fe-, Co-, Zn- and Mn-ferrites or mixed ferrites in either the core or the shell component.[13,42–47] As will be discussed in Sections 3 and 4, the exchange-coupling between both phases plays a crucial role in the outstanding heating efficiencies of these kinds of hybrid systems.[13]

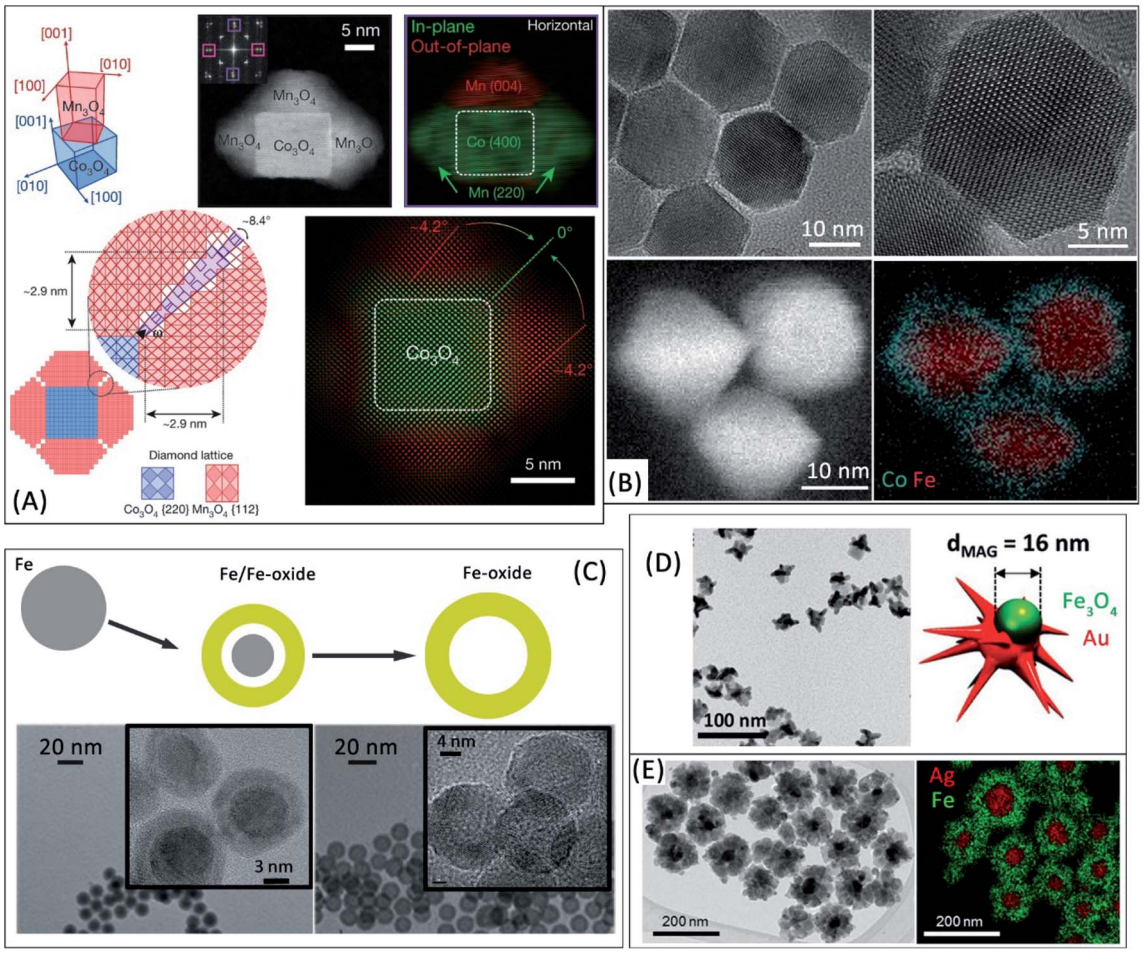

Fig. 1 (A) Design of multigrain Mn_3O_4 shells grown on Co_3O_4 nanocubes. The upper panel shows the orientation relationship between the cubic core and the tetragonal shell by mapping the outer (green) and inner (red) spots of the FFT region (indicated by a purple square) obtained from the associated HAADF-STEM image. The lower panel summarizes the grain boundaries between adjacent Mn_3O_4 grains with a misorientation angle of ~8.4°. Adapted with permission from Nature, ref. 10, Copyright 2020 Nature (B) high-resolution TEM and STEM-EELS elemental mapping images confirm a coherent interface between Fe_3O_4 and $CoFe_2O_4$ in core/shell hybrid nanoparticles. Adapted with permission from ref. 42, Copyright 2020 American Chemical Society (C) evolution from metal Fe to Fe/Fe-oxide core/shell and Fe-oxide hollow nanoparticles and associated TEM images. Adapted with permission from ref. 40, Copyright 2016 Royal Society of Chemistry (D) TEM image of Janus Fe-oxide-Au nanostars. Adapted with permission from ref. 2, Copyright 2020 Wiley-VCH (E) TEM image and EDS elemental mapping of Ag/Fe_3O_4 nanoflowers. Adapted with permission from ref. 14, Copyright 2016 American Chemical Society.

Multiple organic-phase based routes can be adapted to produce core/shell spinel ferrites, being metal oleates and metal acetylacetonates the most common organometallic precursors. The seed-mediated process originally proposed by Sun's group to synthesize Fe_3O_4 NPs with a tunable size between 6 and 20 nm (ref. 30 and 48) can be adapted to synthesize core/shell HNPs with variable core and shell compositions.[43,45,49–51] For example, 12 nm Fe_3O_4 NPs were prepared by the thermal decomposition of Fe(III) acetylacetonate in benzylether assisted by oleic acid, oleylamine and 1,2-hexadecanediol and were used as seeds for the growth of a Zn–Co mixed ferrite layer with variable thickness and composition.[42] In these HNPs, transmission electron microscopy (TEM) studies (summarized in Fig. 1B) reveal a coherent interface with continuous atomic lattice fringes between core and shell thanks to the remarkably low difference between the lattice parameter of the magnetite and the mixed ferrite, below 0.3%. At the same time, electron energy loss spectrum (EELS) images confirm the core/shell architecture of the nanocrystals and the sharp compositional interface between both phases.[42,52]

In another study, Chai *et al.*[53] synthesized FePt/metal-oxides HNPs in a one-pot scheme based on the epitaxial growth of the metal oxide on FePt seeds which were formed earlier in the reaction. In a typical process, the authors mixed a solution containing Pt(II) acetylacetonate, 1,2-hexadecanediol and octadecene with Fe(III) acetylacetonate, oleic acid and oleylamine. As a result of the easier reduction of Pt(II), Pt-rich nuclei are formed at lower temperatures, catalyzing the reduction of the Fe precursor and enabling the formation of FePt particles that act as seeds for the subsequent growth of the oxide phase. Interestingly, the structure can accommodate a large lattice mismatch (~8%) between both components through the introduction of point defects[53] or, eventually, by the formation of grain boundaries in the oxide shell.[54] Alternatively, Sanna

Angotzi *et al.* proposed a two-step approach to synthetize core/shell ferrites, which is based on the hydrolysis of metal oleates under solvothermal conditions using mixtures of 1-pentanol, toluene and water.[44] While controlling the size is probably more difficult as compared to thermal decomposition methods, this approach has the advantage of being easier and less expensive. Although their potential for improving the magnetic heating is still not fully clear, the thermal decomposition synthesis of epitaxially grown HNPs can also be adapted to obtain multi-shell HNPs.[55–57]

2b Hybrid nanostructures through cation-exchange routes

Originally developed for semiconductor nanostructures,[58] an alternative approach for preparing magnetic HNPs relies on cation-exchange (CE) processes.[59–65] CE consists in the partial or total replacement of cations from a nanocrystal structure with other cations solubilized in the dispersion medium, without modifying the original anion sublattice. Although the magnetic properties of HNPs can be tuned in this way, it has been only marginally applied to magnetic metal oxides up to now. A typical CE process consists in mixing pre-prepared nanoparticles with additional metal precursors and surfactants and heating the mixture at temperatures lower than usual organic-phase synthesis values. Former reports showed that the exchange of different transition metal cations occurs over the whole volume of iron oxide nanocrystals,[59] which could be employed to produce hollow nanostructures *via* the Kirkendall effect.[61,65] On the other hand, following studies pointed to the formation of core/shell structures due to the greater exchange rate for cations located closer to the surface.[60] For example, by mixing oleate-capped Fe_3O_4 NPs with $CoCl_2$ previously dissolved in oleylamine, heating the mixture at 200 °C and adding trioctylphosphine, it is possible to exchange part of the Fe atoms in the magnetite by Co cations,[59,60] leading to an increase in the effective anisotropy of the nanocrystals. The main advantage of this method is the ability to tune the magnetic properties without modifying the size and morphology of the original NPs.[9,65] However, the mechanisms behind CE in iron oxides are far from being fully understood, and it has been suggested that the metal oxidation state and the presence of cation vacancies and oxidants in the reaction can play a crucial role in determining the extent of the process and the final product.[60,66] Despite their potential to tune the magnetic properties, only a few works have been devoted to optimizing the heating efficiency of nanostructures through CE-routes,[64] while most studies have focused on the design of HNPs for catalysis and magnetic resonance imaging (MRI) contrast agents.

2c Hybrid nanostructures to functionalize or passivate chemically-unstable cores

Probably the first examples of HNPs have been obtained by the transformation of chemically unstable metallic particles.[67] When exposed to air atmosphere, Fe MNPs are rapidly oxidized,[12,68,69] and a thin iron oxide layer is spontaneously formed leading to core/shell structures, as shown in Fig. 1C. Due to the large magnetic moment of metallic Fe, these Fe/Fe_3O_4 or Fe/γ-Fe_2O_3 architectures are expectedly promising for the development of efficient nanoheaters.[70] However, following a rapid initial passivation, the oxidation of the Fe cores continues and, in some cases, after sufficient time, hollow iron oxide MNPs with much lower magnetization are obtained.[40] As this process occurs much faster in smaller particles (below ~10 nm), better heating powers have been obtained for larger HNPs. Similarly, Famiani *et al.* prepared Fe NPs with tunable size by the continuous injection of $Fe(CO)_5$ to a mixture of 1-octadecene, oleylamine and hexadecylammonium chloride at high temperature.[39] The NPs result in a Fe/Fe-oxide core/shell architecture and can be transferred to water by the exchange of oleate molecules with a dopamine-functionalized amphiphilic polymer. Notably, the authors report that the 18 nm NPs showed a better chemical stability and larger heating powers compared to the 15 nm NPs as a result of a lower oxidation degree.[39] Alternatively, Fe/Fe-oxide core/shell NPs with larger sizes in the range 30–80 nm were prepared by the physical vapor phase condensation route;[71] as discussed by the authors, the presence of a thin FeO interlayer and the core–shell ratio play a critical role in determining the heating efficiency.

Despite the great synthetic control achieved in the last years, HNPs are sometimes obtained due to difficulties in controlling the Fe oxidation state. This is the case of the thermal decomposition of Fe-oleate complexes that can lead to NPs formed by a FeO-rich core and a Fe_3O_4/γ-Fe_2O_3 shell.[72,73] Being antiferromagnetic, the wüstite (FeO) core tends to lower the magnetization and the heating power and, to overcome this drawback, post-processing is usually needed.[73] At the same time, a controlled oxidation of the FeO domains within HNPs can lead to defective-spinel ferrite nanocrystals, which can be employed to optimize the heating power,[74,75] as will be discussed in Section 4.

On the other hand, HNPs can be designed to enhance the chemical stability of MNPs. It was shown, for example, that the epitaxial growth of a Zn-ferrite layer on stoichiometric Fe_3O_4 cores prevented the magnetite oxidation,[52] which was otherwise transformed to γ-Fe_2O_3,[76–78] leading to a decrease in its magnetic anisotropy and magnetization.[41,52] Interestingly, the negligible lattice strain provided by the isostructural Zn-ferrite layer could lower the cation diffusivities,[12,52] hindering the oxidation of Fe_3O_4 cores and recalling the role of epitaxial growth in colloidal chemistry as a tool to control the physical and chemical properties. Another example is HNPs based on Fe-carbides,[79] which can be synthesized by treating palmitic acid and hexadecylamine-stabilized Fe nanocrystals with CO/H_2.[79] The authors showed that a 2 nm-thick oxide layer was initially formed on the surface of the NPs leading to a hybrid Fe carbide-oxide structure that was transferred to water by dopamine-based ligands. Interestingly, the heating powers decreased after 4 months but were still high, suggesting that the Fe carbide-based HNPs could provide a good compromise between chemical stability and high magnetization.[79] Furthermore, by tuning the Fe content in the carbide phase, it is possible to achieve drastically different heating powers,[80] due to variations in the heating mechanisms that govern the process.

In order to be employed in most biomedical applications, the HNPs require a surface functionalization. Since the synthesis methods commonly employed in the synthesis of HNPs lead to hydrophobic particles, the HNPs are usually treated to obtain water-soluble colloids by either an inorganic or an organic coating. In the first case, the HNPs are sometimes formed by an active magnetic core encapsulated in a non-magnetic shell intended to provide chemical stability, to prevent their aggregation by isolating the magnetic cores, or to provide further functionalization. We can highlight, for example, the use of a carbon coating to provide chemical stability and biocompatibility of FeCo particles with remarkably large magnetization,[81] or the coating of iron oxides with a thin SiO_2 shell through a reverse microemulsion method.[82] Alternatively, HNPs can be coated by organic molecules to provide water stability, likewise the surface functionalization of single-phase MNPs.[9] The most common strategies involve the exchange of oleate molecules with hydrophilic ones, such as citrate,[46] tetramethylammonium hydroxide,[42] dopamine-based polymers[39] or methoxy poly (ethylene glycol).[83] Alternatively, the oleate-capped HNPs can be coated with amphiphilic polymers,[47] which have an advantage of avoiding the removal of the original ligands and provide additional functionalization options. It is worth noting that, depending on the nature and characteristics of the coating, the functionalization step can have a variable impact on the magnetic and heating outputs of the material. The interparticle magnetic interactions and therefore the colloidal anisotropy of the MNPs have been shown to depend on the characteristics of the hydrophilic ligands,[84] which can ultimately determine the heating efficiency. For example, it was shown that the heating powers of bimagnetic core/shell HNPs with magnetically softer shells are less sensitive to the ligand-exchange process employed to transfer them to water from non-polar colloids.[42]

2d Synthesis of magnetic-plasmonic hybrid nanoparticles

Other HNPs combine two components that are able to interact independently with external stimuli and contribute simultaneously to the heating power. A typical example is the combination of magnetic and plasmonic entities in a single nanostructure, both able to deliver heat by dissipating the energy from electromagnetic radiation.[20] To provide an efficient local heating, such components should be designed to interact efficiently with the external stimulus. This means that the plasmonic absorption should match the incident light wavelength and that the characteristics of the magnetic entity should be tuned according to the frequency and amplitude of the external field.

To synthetize hybrid iron oxide-metal nanostructures, $Fe(CO)_5$ was decomposed in 1-octadecene and oleic acid on previously formed Au NPs.[85,86] This procedure leads to NPs with low polydispersity and a Janus (two-faced) structure as a result of the formation of (111)/(111) or (111)/(311) Au/Fe-oxide interfaces, with a relatively low lattice mismatch. However, their application to the design of efficient nanoheaters has been limited by the difficulties in achieving, simultaneously, NIR-absorbing metals (preferred due to the lower tissue absorption in this range) and Fe-oxides with appropriate anisotropy and size for magnetic hyperthermia. The latter has recently been accomplished in Janus Au/Fe-oxide HNPs with a magnetic component of either 16 or 20 nm, suitable for magnetic hyperthermia.[2] To further optimize the plasmonic counterpart for photothermal therapies, the authors transformed the morphology of the Au component in a second step by injecting the former particles to a mixture of Au precursors in *N*,*N*-dimethylformamide and polyvinylpyrrolidone to obtain magnetic-Au spiky nanostars (as highlighted in Fig. 1D). Alternatively, Ag/Fe_3O_4 nanoflowers formed by Ag domains encapsulated in aggregated Fe_3O_4 nanocrystals (Fig. 1E) were prepared in a single-step solvothermal process and have shown an enhanced magnetic and optical absorption.[14]

Some efforts have been devoted to identifying the main factors that determine the synthesis of iron oxide-metal (Au or Ag) HNPs.[34,87–89] For example, Guardia *et al.* focused on the behavior of Au/Fe-oxide dimers in magnetic hyperthermia experiments[89] and found that chloride ions can promote the nucleation of iron oxide on the Au NP surface. This strategy was exploited to tune the size and shape of the Janus HNPs, and large heating powers were reported for Fe-oxide domains of 24 nm. Other approaches directly provide water-dispersible HNPs. For example, Curcio *et al.*[90] have recently shown that the iron oxide nanoflowers prepared by the polyol method[91] can be coated with CuS shells, which enable a large photothermal conversion of infrared light. The synthesis is based on the reaction of cupric nitrate with polyvinylpyrrolidone and hydrazine to form a Cu_2O shell on the NPs, which is treated in a second step with ammonium sulfide leading to the sulfidation of the oxide and the formation of a CuS spiky shell.

All the strategies summarized above are not exhaustive, and there could be many more novel chemical methods out there in the research community. However, we have tried to capture the evolution of the field of HNPs, highlighting the important progress that has emerged over the years.

3. Basics of magnetism and heating processes at the nanoscale

3a Fundamentals

Before analyzing the inductive heating of HNPs, it is necessary to review some basic notions on nanomagnetism that will allow us to better understand the different elements involved in the heating of HNPs. In general, MNPs present a size in the range of 1–100 nm, and they can be composed of different magnetic materials such as Fe, Ni, Co, *etc.*[92,93] Nowadays, for biomedical and related applications, most of the MNPs are based on iron oxides, magnetite and maghemite preferentially, due to their good biocompatibility.[94] Although these MNPs can present an ordered internal magnetic structure such as bulk magnetic materials, either Ferromagnetic (FM), Antiferromagnetic (AFM) or Ferrimagnetic (FIM),[92] their magnetic response can be very different. As the size of the MNPs decreases, they become single domains below a certain critical size, and in this situation, each MNP can be considered as a small magnet with a net magnetic

moment resulting from the addition of all the magnetic moments inside the MNP. Most of the MNPs employed for biomedical applications are single domain.[95] The magnetic response of these MNPs depends both on their size and the temperature. However, from the practical viewpoint, the temperatures of interest in this kind of applications are generally close to room temperature. With decreasing size, the magnetic response of the MNPs evolves from a magnetically blocked state to a superparamagnetic (SPM) state. In this SPM state, thermal fluctuations tend to dominate the magnetic response of the MNPs, and their magnetic response is analogous to that of a paramagnet, with zero coercivity and remanence in the measured M–H curves. In biomedical applications, SPM MNPs are often favorable, because, lacking coercivity and remanence, they do not tend to agglomerate in the absence of a magnetic field, which is important to minimize their toxicity and improve their half-life inside the human body.[96,97] However, small SPM nanoparticles also present some risks and limitations[98,99] (*e.g.* crossing the blood brain barrier, low heating efficiency, *etc.*), as we will discuss later.

Apart from the size and composition, there are two other ingredients that define the magnetic response of these MNPs: magnetic anisotropy and interparticle magnetic interactions. Magnetic anisotropy is related to the dependence of magnetic properties on a preferred direction, which in the case of MNPs generally means that their net magnetic moment tends to align in a preferential direction or directions. This preferential alignment can drastically change the magnetic response of the MNPs to an external field, and therefore the shape of their M–H loops, which is crucial in different biomedical applications such as magnetic hyperthermia. In the case of MNPs, four main contributions to the anisotropy can be in principle considered: (i) magnetocrystalline anisotropy, related to the intrinsic crystal structure of the material and generally weaker than the other contributions; (ii) shape anisotropy, related to the shape of the MNPs and their magnetostatic energy; (iii) surface anisotropy, mainly due to local symmetry breaking at the surface of the MNPs and specially relevant at very small sizes; and (iv) exchange anisotropy, often associated to the exchange coupling of different magnetic materials, and therefore, especially relevant in the case of HNPs. Finally, interparticle magnetic interactions are normally of dipolar nature, rapidly decrease with decreasing size of the MNPs, and in general are considered undesirable in biomedical applications, since to they tend to make the nanoparticles agglomerate and they often negatively affect their magnetic response.

Magnetic heating is a general term to refer to the heating of magnetic materials when they are under a high frequency magnetic field. The heating of magnetic materials can be due to hysteresis losses and/or eddy currents. Hysteresis losses are related to the magnetic domains and to the hysteresis loop area of the material. On the other hand, eddy-currents are associated to electromagnetic field induction and lead to Joule heating. In most MNPs, hysteresis losses represent the main heating mechanism and Joule heating can be neglected due the small size of the MNPs. However, for larger magnetic materials, Joule heating should also be considered.[100] When subjected to an external AC field, the net magnetic moments of the MNPs oscillate trying to follow the AC field. However, at high frequencies, part of the electromagnetic energy transferred by the AC field is lost, and these losses are converted into heat. The heating efficiency of the MNPs, also known as Specific Absorption Rate (SAR) or Specific Loss Parameter (SLP), is one of the key parameters in biomedical applications that rely on the heat release. By maximizing the heating efficiency of the MNPs, we can reduce, for example, the dosage of MNPs needed to reach the desired temperature. The SAR or SLP, measured in W g^{-1}, can be determined through either calorimetric or magnetometric methods.[101] In calorimetric methods, the heating curves, Temp *vs.* time, of the MNPs are recorded at a certain AC field, and the SAR can be determined from the initial slope of these heating curves:[102,103]

$$\mathrm{SAR} = \frac{m_\mathrm{s}}{m_\mathrm{n}} C_\mathrm{p} \frac{\Delta T}{\Delta t} \tag{1}$$

where C_p is specific heat of the solvent, m_n is mass of the MNPs, m_s is mass of the solvent, and $\Delta T/\Delta t$ is the initial slope. In magnetometric methods, the SAR is directly obtained from the hysteresis losses. The energy losses are proportional to the area, A, of the AC hysteresis loops (*i.e.* magnetization *vs.* AC magnetic field) described by the magnetic moments of the nanoparticles during the application of the AC field. Therefore, the SAR values can also be obtained from the following equation:[103]

$$\mathrm{SAR} = \frac{f}{c} A = \frac{f}{c} \oint \mu_0 M_\mathrm{t} \mathrm{d}H_\mathrm{t} \tag{2}$$

M_t being the instantaneous magnetization at time t, H_t the amplitude of the AC magnetic field of frequency f at time t, and c the weight concentration of MNPs in the medium. Here we must remark that although the DC hysteresis loops, measured with static magnetic fields, of SPM nanoparticles are anhysteretic, their corresponding AC hysteresis loops can present hysteresis, leading to magnetic losses, due to the high frequencies of the AC fields employed (see Fig. 2A). Although both methods can be used to determine the SAR of the MNPs, they can offer complementary information that comprehends our understanding of the hyperthermic response of the MNPs.

Apart from the SAR, another parameter that is often reported is the so-called intrinsic loss power (ILP), typically measured in nH m^2 kg^{-1}. It was first introduced by Pankhurst *et al.*[104] as a way to try to avoid the intrinsic difficulty to compare SAR values reported in different experiments:

$$\mathrm{ILP} = \frac{\mathrm{SAR}}{fH^2} \tag{3}$$

Although sometimes useful, the ILP assumes a linear and quadratic dependence of the SAR with the field frequency, f, and amplitude, H, which, strictly speaking, is mostly valid for low fields and small SPM NPs.[105] Therefore, the ILPs reported for samples that do not fulfill these requirements should be compared with caution.

In order to optimize the heating output in biomedical applications, it is in principle necessary to try to maximize the

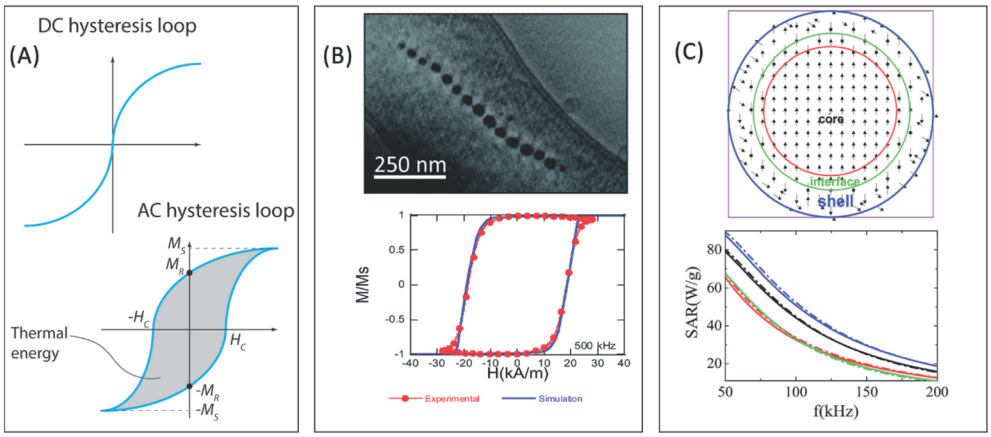

Fig. 2 (A) Comparison between DC and AC hysteresis loops for superparamagnetic nanoparticles. The relevant parameters defining the hysteresis losses (M_s, H_C, and M_R) have been explicitly indicated (B) electron cryotomography image of the chain of magnetosomes of *M. gryphiswaldense* and experimental and simulated AC hysteresis loops measured at 500 kHz for bacteria dispersed in water (25 °C). Reproduced from ref. 122 and 233 under a Creative Commons (CC BY 3.0) License. (C) 2D schematic representation of the different regions in a FM/FIM core/shell spherical nanoparticle, and SAR of core/shell hybrid nanoparticles with different shapes: spherical (black), cubic (red), octahedral (green), and truncated cuboctahedral (blue), and size distributions: log-normal size distribution (solid lines) and uniform particle size (dotted lines). Adapted from ref. 124 with permission from The Royal Society of Chemistry.

hysteresis losses and therefore the SAR of the MNPs. For this, there are different parameters that can be controlled, including external parameters (field amplitude and frequency, dosage, *etc.*) and internal parameters (size, anisotropy, spontaneous magnetization, *etc.*). Since external parameters are limited by medical, technical, and economical factors,[1,105,106] many researchers have focused on tuning the internal parameters, which are related to the MNPs properties. Among them, we can define three main parameters that allows us to control the hysteresis loop area:[107] (i) saturation magnetization (M_s), (ii) effective anisotropy (K), and (iii) volume (V).

The saturation magnetization, M_s, is directly related to the height of the hysteresis loop (see Fig. 2A), and depends on the composition and crystallinity of the MNPs. For example, the bulk M_s value for bulk Fe is 220 emu g^{-1}, while for bulk Fe_3O_4 it is 92 emu g^{-1}. Therefore, by changing the composition of the MNPs we can try to increase their M_s. At the same time, when the size of the MNPs gets reduced, their M_s value tends to decrease due to poor crystallinity, surface disorder and similar effects. Therefore, synthesis routes that allow one to obtain MNPs with good crystallinity are necessary in order to ensure a high M_s value.[92,108]

On the other hand, the effective anisotropy controls the width (given by the coercive field, H_C) and overall shape of the hysteresis loop, and it has been identified as a key parameter.[109–111] By increasing the effective anisotropy of the MNPs, the overall squareness and hysteresis loop area can be increased, provided that the magnitude of the applied AC field is larger than the effective magnetic anisotropy field. As we commented before, the effective anisotropy can be tuned, for example, by changing the shape of the MNPs.

Finally, the volume of the MNPs can also be modified to control the SAR.[112] For small SPM MNPs under low AC fields, the SAR is expected to reach a maximum around 15–20 nm.[113] However, recent works have shown that larger MNPs under higher AC fields can give rise to much higher SAR values than the ones obtained for SPM MNPs.[112] In addition, size uniformity is another important factor to ensure high SAR values.[114]

3b Theoretical modeling

As we commented above, in order to estimate the SAR, we need to calculate the hysteresis loop area described by the net magnetic moment of the MNPs under an external AC field. In the last decades, different numerical models have been developed to estimate these hysteresis losses.[70,115,116] The most basic model was introduced by Rosensweig[113] in 2002, the so-called Linear Response Theory (LRT) or Néel-Brown relaxation model. This model considers two heating mechanisms for the MNPs under an AC field: the Brownian mechanism due to physical rotation of the nanoparticles and the Néel mechanism due to the rotation of the net magnetic moment within the MNP. Each mechanism presents its own characteristic relaxation time, $\tau_N = \tau_0 \exp(E_B/k_BT)$ for the Néel relaxation, and $\tau_B = 3\eta V_h H/k_B T$ for the Brown relaxation, which are dependent on the anisotropy energy barrier E_B, the viscosity of the medium η, and the hydrodynamic volume of the MNPs, V_h. Under an external oscillating field, $H = H_0 \cos \omega t$, the response of the magnetic moment is given by: $M(t) = |\chi| H_0 \cos(\omega t + \phi)$, and the area, A, of the hysteresis loop can be expressed as:

$$A = \mu_0 \pi f H^2 \frac{\omega\tau}{1 + (\omega\tau)^2} \chi_0 \quad (4)$$

where χ_0 is the initial susceptibility of the system, and $1/\tau = (1/\tau_B + 1/\tau_N)$. Although this model has been widely used to calculate the SAR of NPs, its validity is mainly limited to low fields, much smaller than the anisotropy field, and SPM MNPs.[70] In addition, we have to remark that although in the literature some works have distinguished between "relaxation losses" for small

SPM MNPs and "hysteresis losses" for bigger MNPs, this separation is, to some extent, artificial, since in the end all the heat losses are hysteresis losses, as has been explained by Carrey *et al.*[70]

Other more complex models that have been employed to simulate the AC hysteresis loops, include those based on the Stoner-Wolfarth model,[117,118] which describe the heating efficiency of coherently reversed MNPs beyond the SPM regime,[70,119] or those using the Landau–Lifshitz–Gilbert equation for the magnetization dynamics of a single MNP:

$$\frac{\mathrm{d}\hat{\boldsymbol{u}}_\mathrm{m}}{\mathrm{d}t} = \gamma\hat{\boldsymbol{u}}_\mathrm{m} \times \vec{\boldsymbol{B}}_\mathrm{eff} - \alpha\hat{\boldsymbol{u}}_\mathrm{m} \times \frac{\mathrm{d}\hat{\boldsymbol{u}}_\mathrm{m}}{\mathrm{d}t} \quad (5)$$

being α the Gilbert damping constant (dimensionless constant),[120,121] γ the gyromagnetic ratio of free electron, $\vec{\boldsymbol{M}} = M\hat{\boldsymbol{u}}_\mathrm{m}$ the net magnetization vector, $\vec{\boldsymbol{B}}_\mathrm{eff} = -(1/M)\ \partial E/\partial\hat{\boldsymbol{u}}_\mathrm{m}$, and E the energy density of a single MNP. This energy density can contain different contributions, including anisotropy and dipolar interactions, in order to better reproduce the complexity of the magnetic behavior of the MNPs.[122] For example, in a recent work Gandia *et al.* have managed to accurately reproduce, within the framework of the Landau–Lifshitz–Gilbert model, the experimental AC loops measured for magnetosomes (~45 nm truncated octahedral magnetite nanoparticles) forming a chain inside *Magnetospirillum gryphiswaldense* MSR-1 bacteria.[122] (see Fig. 2B).

Apart from the numerical models, Micromagnetic and Monte Carlo simulations have also been employed to simulate the magnetic response of the MNPs and estimate their SAR.[71,123–126] For example, the atomistic-scale modelling has been used to simulate the magnetic response of the spins in the core, the shell, and the interface between both,[124] as shown in Fig. 2C. These individual spins interact with the nearest neighbors *via* Heisenberg interactions given by exchange coupling constants, J. Different anisotropies, K, can be defined depending on the location of the spins. This way, the energy of the system is given by:

$$\begin{aligned} E = &-J_\mathrm{core}\sum_\mathrm{core}\vec{S}_i\vec{S}_j - J_\mathrm{shell}\sum_\mathrm{shell}\vec{S}_i\vec{S}_j - J_\mathrm{IF}\sum_\mathrm{IF}\vec{S}_i\vec{S}_j \\ &- \sum_\mathrm{core}K_\mathrm{core}\left(\vec{S}_i\hat{e}_i\right)^2 - \sum_\mathrm{shell}K_\mathrm{shell}\left(\vec{S}_i\hat{e}_i\right)^2 - \sum_\mathrm{IF}K_\mathrm{IF}\left(\vec{S}_i\hat{e}_i\right)^2 \\ &- \sum_\mathrm{surface}K_\mathrm{surface}\left(\vec{S}_i\hat{e}_i\right)^2 - \vec{H}\sum_i\vec{S}_i \end{aligned} \quad (6)$$

being $\vec{S}_i$ the atomic spin and $\hat{e}_i$ the unit vector in the direction of the easy axis at site i. By defining the energy of the system and using an adequate algorithm, the magnetization behavior of complex MNPs, including HNPs, can be reproduced, and from there on, the SAR values can be calculated.

These numerical models and simulations have been very helpful in order to better understand the relevance of the different mechanisms controlling the heating efficiency of MNPs, and to find new strategies that can improve the current hyperthermia results. Nevertheless, it must always be taken into account the limitations of the models employed, especially when trying to reproduce the complex magnetic behaviors that the MNPs can exhibit during *in vitro* and *in vivo* experiments.[110,127,128]

4. Interface-mediated heating power

In this section, we will go through various interface phenomena that determine the magnetic properties, and often the SARs of HNPs, and are mostly associated with the exchange–coupling at the interface. In addition, we will review recent reports that provide a theoretical frame to rationalize the heating output of HNPs in view of the different interface effects.

4a Exchange–coupling

In the case of HNPs, apart from tuning the shape, size, and composition, the SAR can also be controlled through the exchange coupling of their inorganic components, *i.e.* by tuning their exchange anisotropy.[67] This adds an additional degree of freedom that has proven to be very useful in order to maximize the heating efficiency of the HNPs.[126]

Although first observed in fine particles,[67] most of the theory behind exchange-coupled HNPs has been adapted from studies on thin film bilayers.[26,129,130] Briefly, the strategy consists in combining two inorganic phases with different anisotropy (K) and magnetization (M). If the soft phase (lower K and usually larger M) is smaller than twice the domain wall thickness (δ_h) of the hard phase (larger K and usually lower M), a rigid coupling between both phases is expected.[26,131] A rigid coupling means that the magnetization of both components will reverse at the same field and a smooth hysteresis loop will be observed. On the other hand, an exchange-spring behavior will be observed for larger soft layer thicknesses,[132,133] in which case the soft layer reverses its magnetic moment at a lower field compared to the hard component but returns to its original remanence state due to the exchange interaction. Although the general exchange coupling and associated exchange bias phenomena have been widely exploited for the design of permanent magnets and Magnetic Random-Access Memory (MRAM) applications, it has been much less used for tuning the heating ability of HNPs, probably because it requires overall sizes above the SPM limit, less favorable in biomedical applications. Since δ_h values for typical hard magnetic materials are around 10 nm,[41] most bimagnetic HNPs behave as rigidly-coupled magnets. In this frame, the optimization of SARs depends on a fine-tuning of K and M, which is basically determined by the parameters of the hard (H) and soft (S) components weighted by their volume fraction (f):

$$K = K_\mathrm{H}f_\mathrm{H} + K_\mathrm{S}f_\mathrm{S} \quad (7)$$

$$M = M_\mathrm{H}f_\mathrm{H} + M_\mathrm{S}f_\mathrm{S} \quad (8)$$

As a result, a fine tuning of K can be attained without compromising M, which is a difficult task in single-phase MNPs. In addition, the interface exchange–coupling is responsible for other unusual effects. For example, it was demonstrated that the magnetic moment of a FIM phase can be stabilized above its Curie temperature through a magnetic

proximity effect due to the coupling with an AFM core in HNPs,[134] an approach that was later exploited to overcome the thermal fluctuations of Co/CoO HNPs beyond the CoO Néel temperature by embedding the particles in a NiO matrix.[135]

Both theoretically and experimentally, it has been demonstrated that the combination of different magnetic phases in HNPs[40,136] can improve the response of the MNPs in hyperthermia.[126] Many of these HNPs are based on combinations of hard and soft magnetic ferrite phases in the form of core/shell structures,[45,47,137,138] such as $CoFe_2O_4/NiFe_2O_4$,[139] $Fe_3O_4/CoFe_2O_4$,[140] $Zn_xCo_yFe_zO_4/\gamma$-Fe_2O_3,[141] *etc.* Table 1 summarizes some representative core/shell HNPs, together with the size of their components and the experimental SARs. For example, Noh *et al.*[126,142] used a hard magnetic core and a soft magnetic shell to tune both K and M and increase the hysteresis loop area. In this way, they managed to attain high SAR values of 10 600 W g^{-1} ($H = 460$ Oe, $f = 500$ kHz) in 60 nm core/shell nanocubes of $Zn_{0.4}Fe_{2.6}O_4/CoFe_2O_4$, although such high values are still debated[143] and are far beyond the SPM size range. On the other hand, Simeonidis *et al.*[71] recently reported SARs of 900 W g^{-1} ($H = 300$ Oe, $f = 765$ kHz) in HNPs formed by 15 nm Fe cores covered by a 24 nm-thick Fe_3O_4 shell. In addition, Lavorato *et al.*[42] studied the heating efficiency of the Fe_3O_4/Co_xZn_{1-x}-Fe_2O_4 core/shell HNPs, demonstrating that it can be maximized for $x = 0.25$ and a 3 nm-thick shell layer on a 12 nm core, reaching a maximum value of 2400 W g^{-1} ($H = 800$ Oe, $f = 309$ kHz). As shown in Section 3, the heating mechanism depends strongly on the anisotropy and size of the HNPs; $Fe_3O_4/Co_xZn_{1-x}Fe_2O_4$ core/shell HNPs with variable shell composition and size can provide an insight on the origin of the heating powers in colloids with different viscosities. The authors showed that a reduction in the shell thickness or in the Co/Zn ratio resulted in a transition from a Brown-governed regime to a region governed by a collective behavior, characterized by the formation of chain-like structures.[42]

Most of the hard-soft exchange-coupled HNPs mentioned earlier are based on the introduction of Co into one of the ferrites to achieve a large K_H. However, the incorporation of Co cations in Fe oxides is associated with an increased toxicity[144,145] and are not the best candidates for clinical applications. In this context, Nandwana *et al.*[46] studied a library of different Co-free exchange-coupled HNPs containing Fe-, Zn- and Mn-ferrites and mixed ferrites and showed that the optimization of the shell fraction and composition allowed achieving a large SAR of up to 827 W g^{-1} ($H = 63$ Oe, $f = 300$ kHz). Soft–soft HNPs are gaining interest because it has been demonstrated that to achieve an efficient heat delivery in cells a purely magnetic dissipation is required due to the MNP immobilization in biological media with large viscosities[146,147] and inhibition of Brown dissipation mechanisms.[148] Although not particularly focused on the heating efficiency, an innovative approach to control the effective anisotropy was proposed by Sartori *et al.*[56] by synthesizing core/shell/shell HNPs formed by iron oxides with a Co-doped inner shell layer. The authors argued that this led to a magnetic anisotropy enhancement in rather small

Table 1 Summary of bimagnetic core/shell hybrid nanoparticles, indicating nanocrystal morphology, overall and core sizes, applied frequency (f), field amplitude (H) and experimental heating efficiency parameters. While most SAR and ILP values are expressed per gram of material, the asterisks (*) indicate values reported per mass of metal atoms. Precaution should be taken when comparing ILP values calculated from different reports since the conditions required for the LRT are not always fulfilled

Core/shell HNPs	Morphology	Size (nm)	Core size (nm)	f (kHz)	H (Oe)	SAR (W g^{-1})	ILP (nH m^2 kg^{-1})
Fe/Fe_3O_4 (ref. 39)	Sphere	18.3 ± 1.1	11.4	303	308	696	3.8
Fe/Fe_3O_4 (ref. 234)	Sphere	15	10	177	330	140	1.1
Fe/γ-Fe_2O_3 (ref. 40)	Sphere	14	7.2	310	800	130	0.1
$FePt/Fe_3O_4$ (ref. 151)	Cube	14.7 ± 1.1	4.1	630	236	1210	5.4
$Fe_{2.22}C/Fe_{3-x}O_4$ (ref. 79)	Sphere	15.1 ± 0.9	13	100	470	700	5.0
$Fe_3O_4/CoFe_2O_4$ (ref. 137)	Rock-like	12 ± 1.7	7.7 ± 1.1	97	628	130*	0.5*
$Fe_3O_4/CoFe_2O_4$ (ref. 140)	Sphere	9.9 ± 0.1	7.8 ± 0.1	310	800	461	0.4
$Fe_3O_4/Co_{0.25}Zn_{0.75}Fe_2O_4$ (ref. 42)	Polyhedron	18.2 ± 1.8	12.1 ± 1.3	310	800	2400	1.9
$Fe_3O_4/Co_{0.25}Zn_{0.75}Fe_2O_4$ (ref. 42)	Polyhedron	18.2 ± 1.8	12.1 ± 1.3	310	200	285	3.6
$Fe_3O_4/ZnFe_2O_4$ (ref. 42)	Polyhedron	17.2 ± 1.7	12.1 ± 1.3	310	200	230	2.9
$Fe_3O_4/Zn_{0.5}Co_{0.5}Fe_2O_4$ (ref. 45)	Sphere	9.4 ± 1.4	7.5 ± 2.7	817	200	190	0.9
$Fe_3O_4/MnFe_2O_4$ (ref. 142)	Sphere	15	9	500	469	2795*	4.0*
$CoFe_2O_4/Fe_3O_4$ (ref. 138)	Sphere	12.8	9	183	214	59	1.1
$CoFe_2O_4/Fe_3O_4$ (ref. 235)	Sphere	11.9	8.7	765	300	450	1.0
$CoFe_2O_4/Fe_3O_4$ (ref. 137)	Rock-like	16	10.6	97	628	51*	0.2*
$CoFe_2O_4/MnFe_2O_4$ (ref. 47)	Sphere	12.9 ± 1.4	6.7 ± 1.0	412.5	281	553	2.7
$CoFe_2O_4/MnFe_2O_4$ (ref. 142)	Sphere	15	9	500	469	2280*	3.3*
$CoFe_2O_4/Ni_{0.5}Zn_{0.5}Fe_2O_4$ (ref. 236)	Sphere	9	5	256	377	25	0.1
$MnFe_2O_4/CoFe_2O_4$ (ref. 237)	Sphere	16	10	765	352	160	0.3
$MnFe_2O_4/CoFe_2O_4$ (ref. 142)	Sphere	15	9	500	469	3034	4.4
$Zn_{0.4}Fe_{2.6}O_4/CoFe_2O_4$ (ref. 126)	Cube	70	50	500	474	10 600*	14.9*
$Zn_{0.17}Mn_{0.68}Fe_{1.9}O_4/\gamma$-$Fe_2O_3$ (ref. 141)	Rock-like	9.2	~8	831	300	799	1.7
$Zn_{0.4}Co_{0.6}Fe_2O_4/Zn_{0.4}Mn_{0.6}Fe_2O_4$ (ref. 142)	Sphere	15	9	500	469	3886*	5.6*
$Zn_{0.4}Co_{0.6}Fe_2O_4/Zn_{0.4}Mn_{0.6}Fe_2O_4$ (ref. 83)	Polyhedron	11.2 ± 1.3	7.6 ± 1.4	200	761	1343	1.8

particles mostly formed by Fe-oxides,[56] both interesting conditions for biomedical applications.

It is generally accepted that SPM particles are preferred for minimizing the magnetic interactions at room temperature and preventing toxicity effects associated with particle aggregation. However, there is an alternative approach that utilizes magnetic structures with very low remanence (*e.g.* vortex-like spin arrangements in single-crystal magnetic nanorings[149,150]), which have been also achieved in exchange-coupled cubic $FePt/Fe_3O_4$ core/shell HNPs.[151] Large relaxivity and SAR (up to 1210 W g^{-1} for $H = 236$ Oe and $f = 630$ kHz) make this system suitable for a theranostic (therapy + diagnostic) platform that combines both hyperthermia and MRI.[151]

Apart from the core/shell structure, other different exchange-coupled arrangements of HNPs have also been investigated for magnetic hyperthermia, such as nanoflowers consisting of γ-Fe_2O_3 magnetic grains grown over the surface of $MnFe_2O_4$ core,[152] or Fe_3O_4 MNPs with embedded FeO nanoclusters.[153] In this regard, there is still ongoing research on several possible hetero-structures and assemblies that can allow one to tune of the magnetic properties of the MNPs in order to enhance their biomedical performance.[25,154,155]

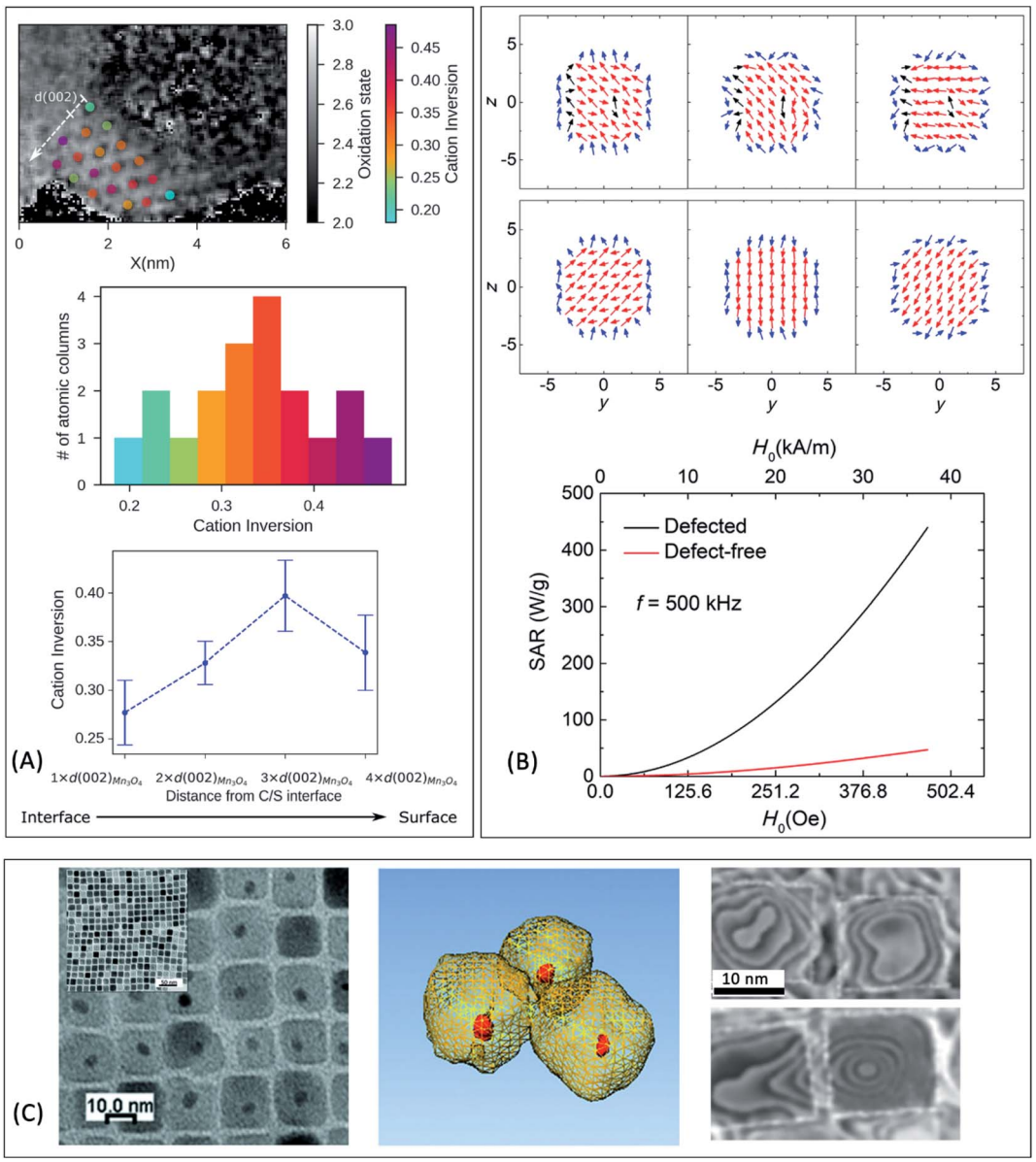

Fig. 3 (A) Cation-inversion gradient in the shell of a Mn_3O_4 domain grown on Fe_3O_4 nanoparticles. Reprinted with permission from ref. 156, Copyright 2018 American Chemical Society (B) Monte Carlo simulations of the spin configurations for spherical defected (upper panel) and defect-free (lower panel) nanoparticles. From left to right the diagrams indicate the configuration under a positive field and two different reversal fields, while core, surface and defect spins are represented in red, blue and black, respectively. The bottom inset indicates the comparison of the simulated SAR values for both cases. Reprinted from ref. 75 under a Creative Commons Attribution 4.0 International Licence (C) $FePt/Fe_3O_4$ core/shell nanocubes: TEM images, 3D-TEM tomography and off-axis electron holography at the remanence state indicating a magnetic vortex magnetic flux configuration. Adapted with permission from ref. 151, Copyright 2018 Wiley-VCH.

4b Novel interface-mediated effects: defective hybrid nanoparticles and imperfect coupling

As the SAR is strongly dependent on the magnetic anisotropy, other interface-mediated effects that modulate the effective anisotropy are expected to have a great importance. However, their interpretation is often challenging and depends on a comprehensive structural and magnetic understanding of the interface. For example, by directly mapping the divalent and trivalent metal atoms through atomic-resolution EELS measurements, Torruella *et al.*[156] demonstrated for the first time a cation inversion gradient at the shell of Fe_3O_4/Mn_3O_4 core/shell HNPs (as highlighted Fig. 3A). By applying a set of different experimental techniques to similar HNPs, it was demonstrated that Fe_3O_4 and Mn_3O_4 are antiferromagnetically-coupled at the interface, accounting for unusual magnetic properties such as a positive exchange bias and an unexpected temperature dependence of K.[11] Such a precise understanding of interface-mediated effects suggests that HNPs offer unexplored ways for tuning the magnetic properties apart from solely the weighted-contribution of their core and shell components. In another report,[157] HNPs formed by Mn_3O_4 domains grown on the corners of Fe_3O_4 prisms have shown unique magnetization reversal modes that are not observed in single-phase MNPs. Interestingly, only a few examples of MNPs with such degree of morphological complexity have been studied[158] even though numerous complex structures have been obtained in other nanomaterials, such as semiconductor and noble metal nanocrystals.[31,159]

TEM studies have shown that metal-oxides HNPs can exhibit a surprisingly sharp interface between both phases.[52,160] While it is accepted that a defect-free interface between two highly crystalline phases maximizes the exchange coupling,[161] it is less clear to what extent an imperfect coupling can tailor the SAR. Some studies suggested that this concept can be realized by introducing non-magnetic atoms to reduce the number of effective bonds at the interface,[162] and that an imperfect coupling can enhance the energy product.[163]

In this context, researchers investigated MNPs obtained by transforming FeO/Fe_3O_4 HNPs into defective-spinel nanocrystals either spontaneously or by mild thermal treatments.[73–75] Interestingly, although the sharp interface between both components is lost after the phase transformation, the defective structures showed promising properties for magnetic hyperthermia. For example, Lak *et al.* showed that the treated MNPs possessed structural defects, with Fe^{2+} deficiencies and FeO subdomains responsible for enhanced SAR values, which were remarkably less dependent on the medium viscosity.[74] In addition, it has been demonstrated that $Fe_xO/Fe_{3-\delta}O_4$ HNPs obtained by the self-passivation of wüstite exhibit pinning defects associated with a tetrahedral distortion in the spinel structure that determine their larger SAR compared to non-defective MNPs.[75] A wüstite core can also be obtained during the synthesis of Zn-substituted ferrites,[164] leading to the introduction of a small Zn fraction in the core and an increased magnetic frustration.

Structural defects are ubiquitous in nanostructures[74,75,165–168] and can have a strong impact on the spin arrangement and magnetization reversal. For example, Fe_3O_4 MNPs obtained by different synthesis routes exhibited anti-phase boundaries,[165,169] which are detrimental to the heating efficiency since they are responsible for a reduction in the magnetic moment. Other structural defects, such as stacking faults, have been associated to an anomalous size dependence of the magnetization and anisotropy of the nanocrystals.[168,170] Depending on the type and density of defects, both an increase[75] or a decrease[74,171] in the overall anisotropy were reported, providing novel ways to optimize the heating output.[17] In sum, the concept of defects nano-engineering is a promising alternative approach for improving the heating efficiency of the MNPs, which thus warrants further work.

4c Can ultrathin shells enhance the heating power?

The magnetization of small MNPs is usually lower than bulk counterparts due to the canting of spins at the surface;[168,172,173] however, core/shell exchange coupled HNPs revealed interface-mediated spin configurations different than their single-phase counterparts.[131,174–176] When the shell layer is ultrathin, *i.e.* a few atomic layers-thick, novel and often unexplained properties have been reported, comprising unexpectedly large anisotropies or coercivity gradients, probably associated to complex spin arrangements at the atomic level.

For example, studies based on polarization-analyzed small angle neutron scattering (SANS) and X-ray magnetic circular dichroism (XMCD) revealed that the magnetic frustration arising from the exchange coupling of thin (~0.5 nm) shells in $Fe_3O_4/Mn_xFe_{3-x}O_4$ HNPs can induce a spin canting in the whole MNP that may be responsible for variations in the hyperthermia output of different MNP systems.[174] In the same line, the impact of the spin arrangement on the heating ability has been demonstrated on single-phase MNPs with similar composition and size but prepared by different methods.[166] Daffé *et al.*[177] measured 7 nm $MnFe_2O_4/CoFe_2O_4$ HNPs with a 0.5 nm-thick shell that confers a strong anisotropy to the soft magnetic core. By employing X-ray element-sensitive spectroscopic techniques with different probe depths, they found a strong gradient in the reversal fields of the Mn ferrite whose origin is still unclear.

Other authors claimed that HNPs with ultrathin shells exhibit an additional source of surface anisotropy due to the spin disorder promoted by the shell layer.[178,179] For example, in ref. 179 the authors reported on Co ferrite nanocubes covered by a thin $MnFe_2O_4$ shell and showed a marked increase in the coercivity compared to bare cores, which was also observed in bare surface-etched cores. However, the mechanisms behind such apparent increase in the coercivity are far from being understood. It was shown that the overall anisotropy of HNPs with ultrathin shells depended on the metal precursor, surfactant and solvent employed in the shell growth, probably due to differences in the surface etching during the synthesis process.[179] This reflects the key role played by the shell formation kinetics and the difficulties in fully assessing the surface properties, since variations in the nature of the organic capping and changes in the oxidation state during the shell growth need to be considered.[52,60,73] We emphasize that more work is

required to understand the behavior of core/shell HNPs with shells approaching a few monolayers and that further studies on this issue should consider the extensive literature on thin film bilayers.[129,130,161,180–183]

4d Modeling the heating efficiency of hybrid nanoparticles

There have been several recent theoretical studies to analyze and better understand the parameters that control the heating efficiency of HNPs. Some of the key parameters that have been identified are:[17,71,184] (i) the ratio between the different magnetic phases present, which can modify the magnetic response from a non-coherent (smaller loop areas) to a fully coherent (larger loop areas) behavior; (ii) the nature and thickness of the interface layer between the magnetic phases, which can modify the interactions between them and therefore the magnetic switching response and the hysteresis loop area; and (iii) the crystallinity of the magnetic phases and the presence of defects/disorder, which will also affect their effective anisotropy and the shape of the loop.

For example, Simeonidis *et al.*,[71] carried out micromagnetic simulations, based on the object-oriented micromagnetic framework (OOMF), to simulate the magnetic behavior of the Fe core and the Fe_3O_4 shell, and analyze the influence of different parameters such as the interface thickness and the polycrystallinity of the shell. Their results indicated that in a coupled core/shell system, non-homogeneous magnetic structures tended to appear, and non-coherent magnetization reversal modes seem to be more adequate to generate large SAR values. On the other hand, Lappas *et al.*[75] used Monte Carlo simulations to investigate how atomic scale defects can modify the heating efficiency in $Fe_xO/Fe_{3-\delta}O_4$ HNPs. The defects' additional anisotropy can lead to exchange randomness, modifying the shape of the AC loops, and improving the SAR of the MNPs under certain conditions. Their results indicated that for small MNPs, the SAR could raise almost tenfold, up to 450 W g^{-1} ($H = 460$ Oe, $f = 500$ kHz), in comparison to non-defected ones (Fig. 3B). Finally, Vasilakaki *et al.*[124] carried out Monte Carlo simulations to estimate the SAR of four different shapes of core/shell HNPs (Fig. 2C). They found that for all shapes and sizes, the FM/FIM core/shell MNPs gave higher SAR values that the pure single-phase ones, and that the MNPs with the truncated cuboctahedral shape exhibited the highest SAR values.

5. Multifunctional hybrid nanoparticles

In the following, we will discuss recent advances devoted to increasing functionalities in HNPs rather than tuning the magnetic properties through the interactions between their components. For a general discussion on multifunctional nanostructures covering magnetic and non-magnetic materials in biomedical applications, the reader is referred *e.g.* to ref. 23 and 25.

5a Getting multifunctional: heating and temperature sensing

One of the most important challenges for the biomedical application of MNPs as heat delivery agents is to achieve a uniform and controllable temperature rise in a certain volume. Therefore, it is desirable to design MNP systems that are able to deliver heat efficiently while providing a temperature signal, which could help, at the same time, to understand fundamental aspects of thermal phenomena in nanomaterials.[185]

Until the last few years, the heating output of MNPs has been solely evaluated by bulk temperature sensing (as described in Section 3) that requires increasing the temperature of the whole NP solution. However, it has been theoretically and experimentally demonstrated that the temperature increment at the surroundings of the MNPs is larger than at the whole medium.[185] Several approaches have been proposed to assess the local temperature, including thermoresponsive fluorescent dyes,[6,186,187] lanthanide complexes[188] and upconverting nanoparticles.[15,16] Some of these reports were based on the design of HNPs with an inductive magnetic heating component combined with a functional counterpart[189] capable of providing a temperature-sensitive response. Given that the temperature sensing probe may interfere the Brownian motion of the NPs by increasing the hydrodynamic size or modifying the interaction with the fluid, particles with a purely Néel-type heating mechanism are preferred and, consequently, most of the proof concepts are based on NPs with low anisotropy.

For example, Dong and Zink[15] designed HNPs formed by a mesoporous SiO_2 loaded with iron oxide and upconverting $NaYF_4$:Yb,Er cores that act as nanoheaters and nanothermometers, respectively. The cores were prepared by organic-phase synthesis routes and were simultaneously transferred to water by using cetyltrimethylammonium bromide (CTAB) and covered with SiO_2 by the base-catalyzed condensation of tetraethylorthosilicate (TEOS). The intensity ratio of two luminescence bands of the upconversion emission spectrum reveals the temperature at the surroundings of the nanocrystals during the magnetic field application, which is larger than the macroscopic temperature rise of the bulk solution,[15] as shown in Fig. 4A. In a similar approach, magneto-optical HNPs that can deliver heat upon the application of an alternating magnetic field while providing a thermal feedback were obtained by encapsulating Fe-oxide and Nd-doped LaF_3 NPs in a polymer.[16] Interestingly, the authors employed the HNPs in *ex vivo* sub-tissue heating experiments with thermal feedback and found that there was no difference between the local temperature increase and the bulk temperature variation, presumably due to a large thermal diffusion in the experimental set-up.

In a recent review, Cazares-Cortes *et al.* compared the temperature rise (ΔT) reported for different systems that employed polymers as spacers between the magnetic heat source and the temperature probe.[22] Even though they compared reports dealing with different MNPs with variable properties and SARs, they showed that ΔT increases rapidly when approaching the surface of the particles (from 6 to 0.5 nm), indicating that there is a strong thermal gradient between the MNPs and the surrounding medium.[22] Such hot spot effect, can be exploited as a temporally and spatially-controlled heat-triggered drug delivery platform[22,186] with minor long-range undesirable effects. However, a recent study showed no

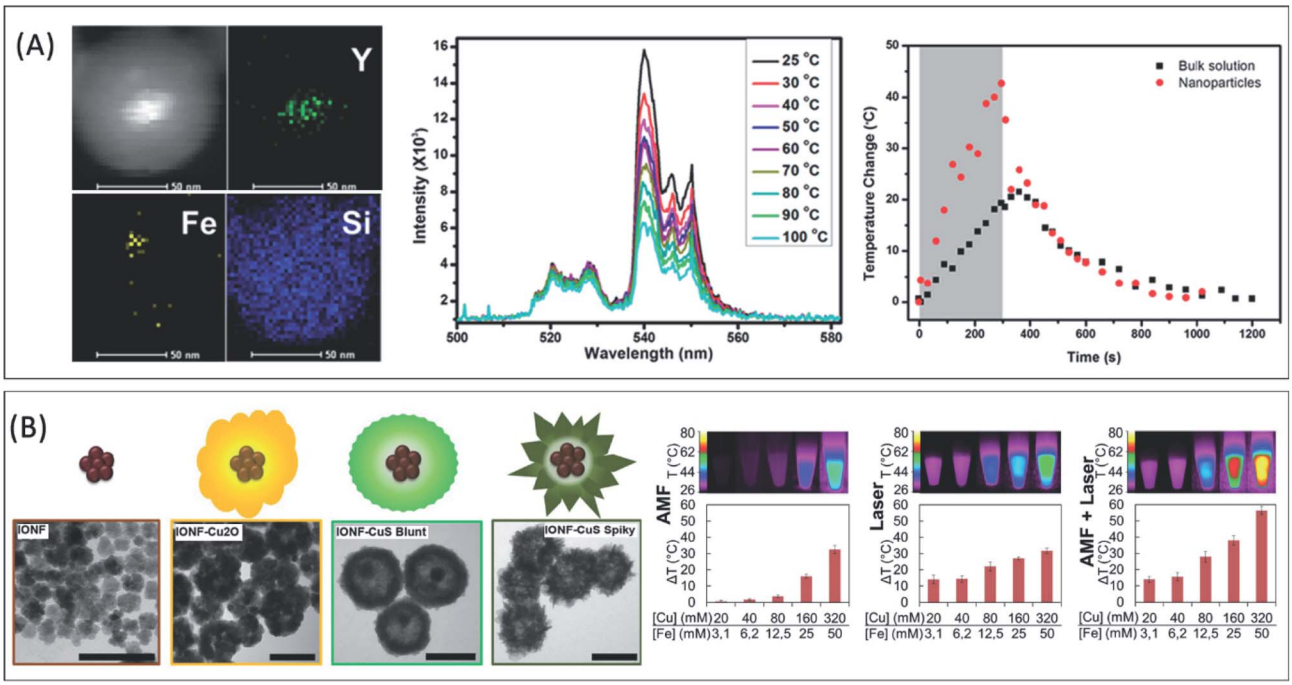

Fig. 4 (A) HAADF-STEM image and elemental mapping of SiO_2-encapsulated Fe-oxide and upconversion $NaYF_4$:Yb^{3+},Er^{3+} nanoparticles (scale bars = 50 nm). Temperature dependence of the excitation spectra and temperature change at the surroundings of the hybrid nanoparticles and at the whole medium under the application of an alternating magnetic field. Adapted with permission from ref. 15, Copyright 2014, American Chemical Society (B) TEM images of Fe-oxide/CuS hybrid nanoflowers and intermediate products (scale bars = 100 nm). Temperature rise (ΔT) as a function of the Fe and Cu concentration for Fe-oxide/CuS hybrid (spiky) nanoflowers at an applied alternating magnetic field (AMF, 471 kHz and 180 Oe), a laser excitation (λ = 1064 nm, 1 W cm^{-2}) or a dual-excitation set-up (AMF + laser). Adapted from ref. 90 under Creative Commons Attribution-NonCommercial 4.0 License.

difference between the thermochromic response of dyes attached to the MNP surface and dyes dispersed in the fluid during radiofrequency magnetic stimulation.[187] The authors pointed to the discrepancy between the existence of such temperature gradients at the surroundings of the NPs and the classical heat transfer theory. While more experimental evidence on local thermal phenomena is crucial to clarify these points, the design and study of hybrid NPs with multiple architectures may play an important role. In addition, HNPs can be also employed as a probe to study the heating mechanisms. For example, fluorescence depolarization experiments were employed to demonstrate that the rotational motion induced by the external field (Brownian relaxation) is negligible in Eu-doped Fe-oxide/SiO_2 core/shell nanoparticles, whose heating process is ruled by a purely Néel-type process.[190]

5b Boosting magnetic heating with light

One of the main drawbacks for the biomedical application of MNP-mediated heating is the high dosage of material needed. For example, to achieve a sufficiently large temperature rise during magnetic hyperthermia therapies *in vivo*, MNP doses are usually orders of magnitude larger than those needed for MRI contrast agents.[22]

A possible approach for increasing the heating efficiency consists in combining two stimuli-responsive materials in HNPs. It is known that local heat can be delivered by the localized surface plasmon resonance through optical excitation of plasmonic NPs, typically Au.[191] In most biomedical applications, giving the minimal absorption of light from biological tissues, it is required for the NPs to absorb energy in the near-infrared (NIR) range, which is achieved by tuning their size and morphology.

In the last years, several studies focused on combining magnetic and plasmonic components in a single HNP,[2,14,22,90,192] which were prepared by a number of different methods, as outlined in Section 2. In a proof of concept, it has been shown that Ag/Fe_3O_4 nanoflowers can act as dual hyperthermia agents demonstrating a synergistic effect that could help to reduce the field or light intensity.[14] However, tuning simultaneously both components to achieve efficient magnetic and optical heating can be challenging, particularly for NIR-absorbing plasmonic components. A possibility to do so is to grow Au on Fe-oxide nanoflowers, which are known to provide large SARs, exploiting the irregular cores morphology to achieve a NIR-absorbing shell.[193] As described in Section 2, a successful attempt is based on Janus HNPs prepared by growing Au nanostars on previously synthesized iron oxide particles with finely tuned sizes for magnetic hyperthermia.[2] A similar approach involves $Cu_{2-x}S$ as the optical component, allowing the large photothermal conversion rates to be achieved in the second NIR window,[90] which is preferred due to the lower light absorption of biological tissue in this range. The photothermal heating

mode has also been demonstrated in Fe/Fe-oxide core/shell NPs[194] and pure Fe-oxide nanostructures,[195] which could also play a relevant role in dual-mode heating platforms, even in the absence of a plasmonic component.

Taken together, these studies suggest that the development of HNPs with magnetic and light-responsive entities can overcome the limitations of purely magnetic nanoheaters. Although a number of reports have demonstrated the increased heating efficiency of a dual approach, the interactions between both components during the application of a magnetic field or light excitation are much less understood[89,196] which warrant further studies. In such kind of particles, the plasmonic surface can provide further functionalization[197,198] and more efforts are needed to clarify, for example, the role of the metallic domain on the heat dissipation during magnetic hyperthermia experiments.

6. Biomedical applications: magnetic hyperthermia and beyond

Magnetic HNPs have been applied in several areas, including magnetic data recording, permanent magnets, microwave absorption, magnetic refrigeration, self-healing materials and tissue engineering.[8,26,199–201] After the initial approval of iron oxide MNPs as contrast agents for MRI[202] and drugs for treatment of iron deficiency,[203] their biomedical applications are expanding to advanced therapies thanks to their high surface to volume ratio, unique tunable properties, colloidal stability, and biocompatibility. The optimization of the heating efficiency would be particularly appealing for biomedical applications based on the local heat generation, including magnetic hyperthermia, while lending the usefulness to heat-triggered drug delivery[3] and heat-mediated cell signaling.[5]

Magnetic hyperthermia is one of the most promising therapies for cancer treatment[1,105,106,204] due to the deep tissue penetration and localized targeted confined heating provided by the MNPs. It is essentially based on the use of MNPs to kill or deactivate cancer cells by releasing heat through the different mechanisms summarized in Section 3. By increasing the temperature, the cancer cells suffer a progressive deterioration that can eventually lead to their apoptosis, or controlled death, which is considered the ideal way to get rid of cancer cells.[105] This is normally achieved by increasing the temperature of the cancer cells to around 42–44 °C, the so-called therapeutic window. Higher temperatures (>50 °C) would lead to a more disruptive destruction of the cancer cell (through thermal ablation) that could pose some risks for the patient.[205] In addition, it has been observed that by raising the temperature in the tumor area, we can improve the efficiency of the therapies commonly employed for cancer treatment, such as chemotherapy and radiotherapy.[206] The advantages of MNPs mediated hyperthermia in comparison with current cancer treatment techniques are rather significant:[96,106] the MNPs, through external magnetic manipulation and adequate coating and surface functionalization, can target the tumor in a more specific way, minimizing the risk of collateral damage; the small size of the MNPs and high penetration of magnetic fields through human tissues are ideal to ensure the efficiency of the treatment in a wide range of tumors; the incorporation of the MNPs into the cancer cells allows for the repetition of the treatment for several days without having to administer additional dosages to the patient, *etc.*

The size, shape and composition of single-phase MNPs have been optimized in the last few years to maximize their heating efficiency.[82,207–209] SARs as large as 2560 W g_{Fe}^{-1} (40 nm Fe_3O_4 MNPs at 260 Oe and 325 kHz),[209] 1111 W g_{Fe}^{-1} (28 nm Fe_3O_4 MNPs at 415 Oe and 150 kHz),[208] 209 W g_{Fe}^{-1} (17 nm Fe_3O_4 MNPs at 126 Oe and 343 kHz)[207] and 3417 W g_{metal}^{-1} (22 nm $Co_{0.03}Mn_{0.28}Fe_{2.7}O_4/SiO_2$ MNPs at 408 Oe and 380 kHz)[82] were reported. Particular attention has been paid to the improvement of the SLPs under clinically relevant conditions; 500 W g_{metal}^{-1} (ILP = 26.8 nH m^2 kg^{-1}) was reported[82] for 22 nm $Zn_{0.3}Fe_{2.7}O_4/SiO_2$ MNPs at 88 Oe and 380 kHz, while 960 W g^{-1} (ILP = 23.4 nH m^2 kg^{-1}) was measured for suspensions of bacterial magnetosomes (30 nm Fe_3O_4 MNPs at 126 Oe and 410 kHz).[210]

As we outlined in the previous sections, HNPs provide an extra degree of freedom to tailor the overall properties and to achieve larger SARs, amongst the highest reported values till date.[42,46,79,126,142] This is evidenced by comparing the values mentioned above with those summarized in Table 1. HNPs can overcome intrinsic limitations of conventional single-phase nanomaterials. For example, the effective anisotropy of HNPs can be controlled without changing the overall particle size,[42,142] and incoherent reversal modes can be promoted by the HNP architecture.[151] While the anisotropy tuning in single-phase MNPs is strongly dependent on small variations in the composition or dopants,[82] which may be difficult to control independently from the particle size, the effective anisotropy of HNPs can be tuned precisely by combining variable fractions of exchange-coupled components with different anisotropies. This is the reason why larger SARs have been reported for HNPs, overcoming, in many cases, those of single-phase MNPs. However, such improvements are at the expense of a more complicated synthesis process and, usually, of introducing additional metal cations into the oxide.

It has been found that the hyperthermia treatment using bimagnetic core/shell $CoFe_2O_4/MnFe_2O_4$ is more efficient in eliminating the U87MG cancer cells in nude mice compared to Feridex and doxorubicin.[142] The SAR has been further improved in cubic shape $MnFe_2O_4/CoFe_2O_4$ core/shell HNPs that enabled a more efficient hyperthermia treatment of drug-resistant cancer cells compared to single-phase ferrite nanocubes.[126] The superior magnetic hyperthermia function of $Zn_{0.4}Co_{0.6}Fe_2O_4/Zn_{0.4}Mn_{0.6}Fe_2O_4$ HNPs conjugated with Zn(II)-bis(dipicolylamine) (bis-ZnDPA) and a chemotherapeutic drug (β-Lap) showed self-amplified apoptosis targeting and inhibited tumor growth.[211]

On the other hand, it has been shown that heat-mediated responses can provide a novel way to act remotely on biological processes. For example, cell functions can be controlled by the gene expression activated by MNPs,[231] and the local heat generated by MNPs under alternating magnetic fields can be

used to stimulate regions inside the brain, opening the control of cellular signaling without the need for permanent implants.[232] As these applications rely on nanomaterials able to deliver heat during the application of an external magnetic field, HNPs optimized for efficient nanoheating or with additional functionalities may pave the way for a deeper control over these processes.

From a theranostic perspective, HNPs that combine optical and magnetic components have gained considerable attention due to their intriguing multifunctional properties ranging from imaging and diagnosis to therapeutics.[212] Several studies have been conducted especially with Fe_3O_4/Au nanostructures using simultaneous alternating magnetic field and laser irradiation, showing enhanced dual heating efficiency[2,193,213] whereas, Au/Fe_3O_4 nanoparticles were used for magnetic field-guided photothermal therapy.[214,215] Au-decorated Fe_3O_4 nanoparticles have shown an enhanced dual magneto and photothermal response while also being a controlled anticancer drug vehicle.[216] Fan *et al.* showed highly selective, targeted diagnosis, isolation and irreparable cancer cell damage using aptamer conjugated Fe_3O_4/Au nanoparticles when irradiating with 670 nm light at 2.5 W cm^{-2} for 10 min.[217] Recently, it has been shown that magneto-plasmonic Fe_3O_4/Au showed a remarkable improvement in therapy of glioma cells.[218] PEGylated Fe/Fe_3O_4 NPs, showed magnetic targeting using MRI and near-infrared photothermal therapy.[194] Results on the photothermal efficiency of PEGylated Fe/Fe_3O_4 HNPs showed a comparable efficiency with Au nanorods. Later, in 2016 Espinosa *et al.* reported on an extremely large SAR of 5000 W g^{-1} in iron oxide nanocubes by dual mode alternating magnetic field and near-infrared laser irradiation.[195] Magneto-plasmonic Fe_3O_4/Au nanoparticles were also used for dual-mode magnetic resonance and computed tomography imaging applications.[219–222]

Beyond magnetic hyperthermia, there has also been an increasing attention to the use of HNPs for novel MRI contrast agents. SPM iron oxide MNPs have been one of the most studied nanomaterials to this end, because of the decrease in the water protons transverse relaxation time (T_2) mediated by the magnetic moment.[202] This leads to a rise in the transverse relaxivity ($r_2 = 1/T_2$) that increases the negative contrast. In this line, the ferromagnetic cores in bimagnetic core/shell Fe/Fe_3O_4 could enhance the overall magnetic moment, while the SPM shell could reduce inter-particle aggregation.[223–227] Thus, this kind of HNPs conserve high r_2, interesting for MRI-based imaging; however, as we pointed out in Section 2, their magnetic properties are degraded with time. Furthermore, Cardona *et al.* reported r_2 values higher than 300 mM^{-1} s^{-1} at 1.5 T, and cell viability at concentrations as high as 0.5 mg mL^{-1} for bimagnetic $Zn_{0.5}Mn_{0.5}Fe_2O_4$/Fe_3O_4 core/shell HNPs,[227] while T_1–T_2 dual-modal contrast agents have also been realized using Fe_3O_4/MnO and Fe_3O_4/Gd_2O_3 HNPs.[228–230]

7. Concluding remarks and outlook

The novel HNPs synthesized over the past decade by different methods have shown nanointerfaces with chemical and physical properties that cannot be attained in single-phase MNPs, and have been rationalized thanks to the framework provided by epitaxial growth-directed methods and advanced characterization techniques. Although several advances have been realized on semiconductor and metal-based NPs, further work is needed on defect-engineering approaches for tuning the magnetic properties in view of their biomedical applications. While it is challenging to achieve a fine control over the nature and density of crystal defects, new synthesis methods and characterization tools are being developed to achieve this goal and can have an important role in improving the heating power of MNPs. Similarly, we envision that there is still room to explore the magnetic properties of HNPs obtained through cation-exchange routes, particularly for NPs with complex morphologies. Regarding HNPs obtained by the controlled oxidation of chemically unstable cores such as Fe or FeCo, we emphasize that further studies on the kinetics of the oxidation process are needed to evaluate if a compromise between a large magnetization and a low chemical stability is advantageous for an efficient and robust heat delivery.

Currently, the most powerful aspect of magnetic HNPs is probably the new properties that emerge from interface-mediated phenomena, which are absent in single-phase nanomaterials. The interface exchange coupling has been employed to finely tune the anisotropy and magnetization of HNPs providing an additional degree of freedom beyond the composition, size and shape: overall exchange-coupled systems now exhibit large heating powers of a few kW g^{-1} ($\sim$1 kW g^{-1} for biomedically safe magnetic fields). Recent results have shown that unexpected properties arise from imperfectly coupled interfaces, which can be obtained *e.g.* by the transformation of FeO/Fe_3O_4 core/shell HNPs into single-phase defective spinels that exhibit heating powers less sensitive to the magnetic interactions and larger than their defect-free counterparts. We highlight the importance of advanced characterization techniques sensitive to the interface at the atomic level to show the full potential of novel systems in the future. Some examples include advanced TEM techniques, EELS and strain mapping with atomic-resolution at the interface, as well as magnetic state-sensitive XMCD and SANS.

Apart from bimagnetic structures, HNPs formed by magnetic and plasmonic components exhibit large heating powers under dual magnetic field and infrared light excitation. Although the synthesis processes required to tune independently the size and shape of both components are not straightforward, recent papers have shown that those structures can be advantageous to overcome the limitations of magnetic or photothermal heating, *i.e.* low heating power and poor tissue penetration, respectively. Future works on these materials should consider the interactions between magnetic and plasmonic components, such as the heat dissipation effect of the plasmonic phase during the magnetic excitation, which have not been fully explored yet. Other structures have shown the remarkable ability of sensing the temperature at the surroundings of the HNPs during the magnetic field excitation, which would provide additional data to understand local heating effects. Finally, we would like to remark that although most of the research on the heating ability of HNPs focused on the magnetic hyperthermia therapies, other

biomedical applications based on local heating effects (such as magnetothermal brain stimulation and heat-induced gene expression) can benefit from novel systems with enhanced heating abilities and functionalities.

Conflicts of interest

There are no conflicts to declare.

Acknowledgements

GCL acknowledges ANPCyT Argentina (PICT 2018-3442) for financial support. JAM acknowledges Ministry of Science and Innovation (Spain) for funding under the project number MAT2017-83631-C3-R. Work at USF was supported by U.S. Department of Energy, Office of Basic Energy Sciences, Division of Materials Science and Engineering under Grant No. DE-FG02-07ER46438. The work at PU was supported by the Vietnam National Foundation for Science and Technology Development (NAFOSTED) under Grant number 103.02-2019.314.

References

1 C. Blanco-Andujar, F. J. Teran and D. Ortega, in *Iron Oxide Nanoparticles for Biomedical Applications*, Elsevier, 2018, pp. 197–245.
2 A. Espinosa, J. Reguera, A. Curcio, Á. Muñoz-noval, C. Kuttner, A. Van De Walle, L. M. Liz-marzán and C. Wilhelm, *Small*, 2020, **1904960**, 1–14.
3 E. Guisasola, A. Baeza, L. Asín, J. M. de la Fuente and M. Vallet-Regí, *Small Methods*, 2018, **1800007**, 1800007.
4 W. Chen, C. A. Cheng and J. I. Zink, *ACS Nano*, 2019, **13**, 1292–1308.
5 J. Moon, M. G. Christiansen, S. Rao, C. Marcus, D. C. Bono, D. Rosenfeld, D. Gregurec, G. Varnavides, P.-H. Chiang, S. Park and P. Anikeeva, *Adv. Funct. Mater.*, 2020, **2000577**, 2000577.
6 H. Huang, S. Delikanli, H. Zeng, D. M. Ferkey and A. Pralle, *Nat. Nanotechnol.*, 2010, **5**, 602–606.
7 C. Niether, S. Faure, A. Bordet, J. Deseure, M. Chatenet, J. Carrey, B. Chaudret and A. Rouet, *Nat. Energy*, 2018, **3**, 476–483.
8 Y. Yang, J. He, Q. Li, L. Gao, J. Hu, R. Zeng, J. Qin, S. X. Wang and Q. Wang, *Nat. Nanotechnol.*, 2019, **14**, 151–155.
9 L. Wu, A. Mendoza-Garcia, Q. Li and S. Sun, *Chem. Rev.*, 2016, **116**, 10473–10512.
10 M. H. Oh, M. G. Cho, D. Y. Chung, I. Park, Y. P. Kwon, C. Ophus, D. Kim, M. G. Kim, B. Jeong, X. W. Gu, J. Jo, J. M. Yoo, J. Hong, S. McMains, K. Kang, Y. E. Sung, A. P. Alivisatos and T. Hyeon, *Nature*, 2020, **577**, 359–363.
11 M. Estrader, A. López-Ortega, S. Estradé, I. V Golosovsky, G. Salazar-Alvarez, M. Vasilakaki, K. N. Trohidou, M. Varela, D. C. Stanley, M. Sinko, M. J. Pechan, D. J. Keavney, F. Peiró, S. Suriñach, M. D. Baró and J. Nogués, *Nat. Commun.*, 2013, **4**, 2960.
12 A. Pratt, L. Lari, O. Hovorka, A. Shah, C. Woffinden, S. P. Tear, C. Binns and R. Kröger, *Nat. Mater.*, 2013, **13**, 26–30.
13 J.-H. Lee, J. Jang, J. Choi, S. H. Moon, S. Noh, J. Kim, J.-G. Kim, I.-S. Kim, K. I. Park and J. Cheon, *Nat. Nanotechnol.*, 2011, **6**, 418–422.
14 R. Das, N. Rinaldi-Montes, J. Alonso, Z. Amghouz, E. Garaio, J. A. Garcia, P. Gorria, J. A. Blanco, M.-H. Phan and H. Srikanth, *ACS Appl. Mater. Interfaces*, 2016, **8**, 25162–25169.
15 J. Dong and J. I. Zink, *ACS Nano*, 2014, **8**, 5199–5207.
16 D. H. Ortgies, F. J. Teran, U. Rocha, L. de la Cueva, G. Salas, D. Cabrera, A. S. Vanetsev, M. Rähn, V. Sammelselg, Y. V. Orlovskii and D. Jaque, *Adv. Funct. Mater.*, 2018, **1704434**, 1704434.
17 A. Lak, S. Disch and P. Bender, 2020, ArXiv:2006.06474.
18 R. M. Fratila and J. M. De La Fuente, *Nanomaterials for Magnetic and Optical Hyperthermia Applications*, Elsevier, 2018.
19 S. Noh, S. H. Moon, T.-H. Shin, Y. Lim and J. Cheon, *Nano Today*, 2017, **13**, 61–76.
20 S. K. Sharma, N. Shrivastava, F. Rossi, L. D. Tung and N. T. K. Thanh, *Nano Today*, 2019, **29**, 100795.
21 S. Shams, M. Ghazanfari and C. Schmitz-Antoniak, *Nanomaterials*, 2019, **9**, 97.
22 E. Cazares-Cortes, S. Cabana, C. Boitard, E. Nehlig, N. Griffete, J. Fresnais, C. Wilhelm, A. Abou-Hassan and C. Ménager, *Adv. Drug Delivery Rev.*, 2019, **138**, 233–246.
23 L.-S. Lin, J. Song, H.-H. Yang and X. Chen, *Adv. Mater.*, 2018, **30**, 1704639.
24 N. Ž. Knežević, I. Gadjanski and J.-O. Durand, *J. Mater. Chem. B*, 2019, **7**, 9–23.
25 D. Kim, K. Shin, S. G. Kwon and T. Hyeon, *Adv. Mater.*, 2018, **22**, 1802309.
26 A. López-Ortega, M. Estrader, G. Salazar-Alvarez, A. G. Roca and J. Nogués, *Phys. Rep.*, 2015, **553**, 1–32.
27 A.-H. Lu, E. L. Salabas and F. Schüth, *Angew. Chem., Int. Ed.*, 2007, **46**, 1222–1244.
28 S. G. Kwon, Y. Piao, J. Park, S. Angappane, Y. Jo, N. M. Hwang, J. G. Park and T. Hyeon, *J. Am. Chem. Soc.*, 2007, **129**, 12571–12584.
29 X. Peng, M. C. Schlamp, A. V. Kadavanich and A. P. Alivisatos, *J. Am. Chem. Soc.*, 1997, **119**, 7019–7029.
30 S. Sun, H. Zeng, D. B. Robinson, S. Raoux, P. M. Rice, S. X. Wang and G. Li, *J. Am. Chem. Soc.*, 2004, **126**, 273–279.
31 C. Tan, J. Chen, X.-J. Wu and H. Zhang, *Nat. Rev. Mater.*, 2018, **3**, 17089.
32 J. Lee, J. Yang, S. G. Kwon and T. Hyeon, *Nat. Rev. Mater.*, 2016, **1**, 16034.
33 J. Zhang, Y. Tang, K. Lee and M. Ouyang, *Science*, 2010, **327**(80), 1634–1638.
34 E. Fantechi, A. G. Roca, B. Sepúlveda, P. Torruella, S. Estradé, F. Peiró, E. Coy, S. Jurga, N. G. Bastús, J. Nogués and V. Puntes, *Chem. Mater.*, 2017, **29**, 4022–4035.
35 J. Reguera, D. Jiménez De Aberasturi, N. Winckelmans, J. Langer, S. Bals and L. M. Liz-Marzán, *Faraday Discuss.*, 2016, **191**, 47–59.

36 *Epitaxial Growth Part A*, ed. J. Matthews, Elsevier, 1975.
37 R. Nickel, M. R. Kazemian, Y. Wroczynskyj, S. Liu and J. Van Lierop, *Nanoscale*, 2020, **12**, 4328–4333.
38 J. Liu and J. Zhang, *Chem. Rev.*, 2020, **120**, 2123–2170.
39 S. Famiani, A. P. LaGrow, M. O. Besenhard, S. Maenosono and N. T. K. Thanh, *Chem. Mater.*, 2018, **30**, 8897–8904.
40 Z. Nemati, J. Alonso, H. Khurshid, M. H. Phan and H. Srikanth, *RSC Adv.*, 2016, **6**, 38697–38702.
41 J. M. D. Coey, *Magnetism and magnetic materials*, Cambridge University Press, 2010.
42 G. C. Lavorato, R. Das, Y. Xing, J. Robles, F. J. Litterst, E. Baggio-Saitovitch, M. Phan and H. Srikanth, *ACS Appl. Nano Mater.*, 2020, **3**, 1755–1765.
43 Q. Song and Z. J. Zhang, *J. Am. Chem. Soc.*, 2012, **134**, 10182–10190.
44 M. Sanna Angotzi, A. Musinu, V. Mameli, A. Ardu, C. Cara, D. Niznansky, H. L. Xin and C. Cannas, *ACS Nano*, 2017, **11**, 7889–7900.
45 F. Fabris, E. Lima, E. De Biasi, H. E. Troiani, M. Vásquez Mansilla, T. E. Torres, R. Fernández Pacheco, M. R. Ibarra, G. F. Goya, R. D. Zysler and E. L. Winkler, *Nanoscale*, 2019, **11**, 3164–3172.
46 V. Nandwana, R. Zhou, J. Mohapatra, S. Kim, P. V. Prasad, J. P. Liu and V. P. Dravid, *ACS Appl. Mater. Interfaces*, 2018, **10**, 27233–27243.
47 Q. Zhang, I. Castellanos-Rubio, R. Munshi, I. Orue, B. Pelaz, K. I. Gries, W. J. Parak, P. del Pino and A. Pralle, *Chem. Mater.*, 2015, **27**, 7380–7387.
48 S. Sun and H. Zeng, *J. Am. Chem. Soc.*, 2002, **124**, 8204–8205.
49 X. Sun, N. F. Huls, A. Sigdel and S. Sun, *Nano Lett.*, 2012, **12**, 246–251.
50 D. Lee, H. Koo, I. Sun, J. H. Ryu, K. Kim and I. C. Kwon, *Chem. Soc. Rev.*, 2012, **41**, 2656–2672.
51 G. C. Lavorato, E. Lima Jr, D. Tobia, D. Fiorani, H. E. Troiani, R. D. Zysler and E. L. Winkler, *Nanotechnology*, 2014, **25**, 355704.
52 G. C. Lavorato, A. A. Rubert, Y. Xing, R. Das, J. Robles, F. J. Litterst, E. Baggio-Saitovitch, M. Phan, H. Srikanth, C. Vericat and M. H. Fonticelli, *Nanoscale*, 2020, **12**, 13626–13636.
53 Y. Chai, F. Feng, Q. Li, C. Yu, X. Feng, P. Lu, X. Yu, M. Ge, X. Wang and L. Yao, *J. Am. Chem. Soc.*, 2019, **141**, 3366–3370.
54 W. I. Liang, X. Zhang, Y. Zan, M. Pan, C. Czarnik, K. Bustillo, J. Xu, Y. H. Chu and H. Zheng, *J. Am. Chem. Soc.*, 2015, **137**, 14850–14853.
55 G. Salazar-Alvarez, H. Lidbaum, A. López-Ortega, M. Estrader, K. Leifer, J. Sort, S. Suriñach, M. D. Baró and J. Nogués, *J. Am. Chem. Soc.*, 2011, **133**, 16738–16741.
56 K. Sartori, F. Choueikani, A. Gloter, S. Begin-Colin, D. Taverna and B. P. Pichon, *J. Am. Chem. Soc.*, 2019, **141**, 9783–9787.
57 V. Gavrilov-Isaac, S. Neveu, V. Dupuis, D. Taverna, A. Gloter and V. Cabuil, *Small*, 2015, **11**, 2614–2618.
58 L. De Trizio and L. Manna, *Chem. Rev.*, 2016, **116**, 10852–10887.
59 M. Sytnyk, R. Kirchschlager, M. I. Bodnarchuk, D. Primetzhofer, D. Kriegner, H. Ennser, J. Stangl, P. Bauer, M. Voith, A. Hassel, F. Krumeich, F. Ludwig, A. Meingast, G. Kothleitner, M. V Kovalenko and W. Heiss, *Nano Lett.*, 2013, 1–13.
60 S. Lentijo-Mozo, D. Deiana, E. Sogne, A. Casu and A. Falqui, *Chem. Mater.*, 2018, **30**, 8099–8112.
61 L. Tian, X. Yang, P. Lu, I. D. Williams, C. Wang, S. Ou, C. Liang and M. Wu, *Inorg. Chem.*, 2008, **47**, 5522–5524.
62 Z. Luo, S. Martí-Sànchez, R. Nafria, G. Joshua, M. De La Mata, P. Guardia, C. Flox, C. Martínez-Boubeta, K. Simeonidis, J. Llorca, J. R. Morante, J. Arbiol, M. Ibáñez and A. Cabot, *ACS Appl. Mater. Interfaces*, 2016, **8**, 29461–29469.
63 Z. Zhao, X. Chi, L. Yang, R. Yang, B. W. Ren, X. Zhu, P. Zhang and J. Gao, *Chem. Mater.*, 2016, **28**, 3497–3506.
64 J. Mohapatra, M. Xing and J. P. Liu, *AIP Adv.*, 2018, **8**, 3–8.
65 M. H. Oh, T. Yu, S. H. Yu, B. Lim, K. T. Ko, M. G. Willinger, D. H. Seo, B. H. Kim, M. G. Cho, J. H. Park, K. Kang, Y. E. Sung, N. Pinna and T. Hyeon, *Science*, 2013, **340**(80), 964–968.
66 A. López-Ortega, A. G. Roca, P. Torruella, M. Petrecca, S. Estradé, F. Peiró, V. Puntes and J. Nogués, *Chem. Mater.*, 2016, **28**, 8025–8031.
67 W. H. Meiklejohn and C. P. Bean, *Phys. Rev.*, 1956, **102**, 1413.
68 T. Hyeon, *Chem. Commun.*, 2003, 927–934.
69 Z. Nemati, H. Khurshid, J. Alonso, M. H. Phan, P. Mukherjee and H. Srikanth, *Nanotechnology*, 2015, **26**, 405705.
70 J. Carrey, B. Mehdaoui and M. Respaud, *J. Appl. Phys.*, 2011, **109**, 083921.
71 K. Simeonidis, C. Martinez-Boubeta, D. Serantes, S. Ruta, O. Chubykalo-Fesenko, R. Chantrell, J. Oró-Solé, L. Balcells, A. S. Kamzin, R. A. Nazipov, A. Makridis and M. Angelakeris, *ACS Appl. Nano Mater.*, 2020, **3**, 4465–4476.
72 L. M. Bronstein, X. Huang, J. Retrum, A. Schmucker, M. Pink, B. D. Stein and B. Dragnea, *Chem. Mater.*, 2007, **19**, 3624–3632.
73 F. Crippa, L. Rodriguez-Lorenzo, X. Hua, B. Goris, S. Bals, J. S. Garitaonandia, S. Balog, D. Burnand, A. M. Hirt, L. Haeni, M. Lattuada, B. Rothen-Rutishauser and A. Petri-Fink, *ACS Appl. Nano Mater.*, 2019, **2**, 4462–4470.
74 A. Lak, M. Cassani, B. T. Mai, N. Winckelmans, D. Cabrera, E. Sadrollahi, S. Marras, H. Remmer, S. Fiorito, L. Cremades-Jimeno, F. J. Litterst, F. Ludwig, L. Manna, F. J. Teran, S. Bals and T. Pellegrino, *Nano Lett.*, 2018, **18**, 6856–6866.
75 A. Lappas, G. Antonaropoulos, K. Brintakis, M. Vasilakaki, K. N. Trohidou, V. Iannotti, G. Ausanio, A. Kostopoulou, M. Abeykoon, I. K. Robinson and E. S. Bozin, *Phys. Rev. X*, 2019, **9**, 41044.
76 L. K. Bogart, C. Blanco-Andujar and Q. A. Pankhurst, *Appl. Phys. Lett.*, 2018, **113**, 133701.
77 S. P. Schwaminger, D. Bauer, P. Fraga-García, F. E. Wagner and S. Berensmeier, *CrystEngComm*, 2017, **19**, 246–255.

78 R. M. Cornell and U. Schwertmann, *The Iron Oxides: Structure, Properties, Reactions, Occurrences and Uses*, Wiley-VCH, Wienheim, 2nd edn, 2003.
79 A. Bordet, R. F. Landis, Y. Lee, G. Y. Tonga, J. M. Asensio, C.-H. Li, P.-F. Fazzini, K. Soulantica, V. M. Rotello and B. Chaudret, *ACS Nano*, 2019, **13**, 2870–2878.
80 J. M. Asensio, J. Marbaix, N. Mille, L.-M. Lacroix, K. Soulantica, P.-F. Fazzini, J. Carrey and B. Chaudret, *Nanoscale*, 2019, **11**, 5402–5411.
81 G. Song, M. Kenney, Y.-S. Chen, X. Zheng, Y. Deng, Z. Chen, S. X. Wang, S. S. Gambhir, H. Dai and J. Rao, *Nat. Biomed. Eng.*, 2020, **4**, 325–334.
82 S. He, H. Zhang, Y. Liu, F. Sun, X. Yu, X. Li, L. Zhang, L. Wang, K. Mao, G. Wang, Y. Lin, Z. Han, R. Sabirianov and H. Zeng, *Small*, 2018, **14**, 1–9.
83 L. Wang, Y. Yan, M. Wang, H. Yang, Z. Zhou, C. Peng and S. Yang, *J. Mater. Chem. B*, 2016, **4**, 1908–1914.
84 L. Gutiérrez, L. De Cueva, M. Moros and E. Mazarío, *Nanotechnology*, 2019, **30**, 112001.
85 C. Wang, H. Yin, S. Dai and S. Sun, *Chem. Mater.*, 2010, **22**, 3277–3282.
86 G. Jiang, Y. Huang, S. Zhang, H. Zhu, Z. Wu and S. Sun, *Nanoscale*, 2016, **8**, 17947–17952.
87 P. Tancredi, L. S. da Costa, S. Calderon, O. Moscoso-Londoño, L. M. Socolovsky, P. J. Ferreira, D. Muraca, D. Zanchet and M. Knobel, *Nano Res.*, 2019, **12**, 1781–1788.
88 J. Zeng, M. Gong, D. Wang, M. Li, W. Xu, Z. Li, S. Li, D. Zhang, Z. Yan and Y. Yin, *Nano Lett.*, 2019, **19**, 3011–3018.
89 P. Guardia, S. Nitti, M. Materia, G. Pugliese, N. Yaacoub, J.-M. Grenèche, C. Lefevre, L. Manna and T. Pellegrino, *J. Mater. Chem. B*, 2017, **5**, 4587–4594.
90 A. Curcio, A. K. A. Silva, S. Cabana, A. Espinosa, B. Baptiste, N. Menguy, C. Wilhelm and A. Abou-Hassan, *Theranostics*, 2019, **9**, 1288–1302.
91 P. Hugounenq, M. Levy, D. Alloyeau, L. Lartigue, E. Dubois, V. Cabuil, C. Ricolleau, S. Roux, C. Wilhelm, F. Gazeau and R. Bazzi, *J. Phys. Chem. C*, 2012, **116**, 15702–15712.
92 J. Alonso, J. M. Barandiarán, L. Fernández Barquín and A. García-Arribas, in *Magnetic Nanostructured Materials: From Lab to Fab*, Elsevier, 2018, pp. 1–40.
93 N. A. Frey, S. Peng, K. Cheng and S. Sun, *Chem. Soc. Rev.*, 2009, **38**, 2532.
94 A. K. Gupta and M. Gupta, *Biomaterials*, 2005, **26**, 3995–4021.
95 Q. A. Pankhurst, J. Connolly, S. K. Jones and J. Dobson, *J. Phys. D: Appl. Phys.*, 2003, **36**, R167–R181.
96 S. Laurent, S. Dutz, U. O. Häfeli and M. Mahmoudi, *Adv. Colloid Interface Sci.*, 2011, **166**, 8–23.
97 M. Mahmoudi, S. Sant, B. Wang, S. Laurent and T. Sen, *Adv. Drug Delivery Rev.*, 2011, **63**, 24–46.
98 N. Singh, G. J. S. Jenkins, R. Asadi and S. H. Doak, *Nano Rev.*, 2010, **1**, 5358.
99 T. Neuberger, B. Schöpf, H. Hofmann, M. Hofmann and B. Von Rechenberg, *J. Magn. Magn. Mater.*, 2005, **293**, 483–496.
100 I. Morales, D. Archilla, P. de la Presa, A. Hernando and P. Marin, *Sci. Rep.*, 2020, **10**, 602.
101 M. R. Z. Kouhpanji and B. J. H. Stadler, *Sensors*, 2020, **20**, 2554.
102 A. Makridis, S. Curto, G. C. Van Rhoon, T. Samaras and M. Angelakeris, *J. Phys. D: Appl. Phys.*, 2019, **52**, 255001.
103 I. Andreu and E. Natividad, *Int. J. Hyperthermia*, 2013, **29**, 739–751.
104 M. Kallumadil, M. Tada, T. Nakagawa, M. Abe, P. Southern and Q. A. Pankhurst, *J. Magn. Magn. Mater.*, 2009, **321**, 1509–1513.
105 D. Ortega Ponce and Q. Pankhurst, in *Nanoscience*, ed. P. O'Brien, Royal Society of Chemistry, 2012, pp. 60–88.
106 E. A. Périgo, G. Hemery, O. Sandre, D. Ortega, E. Garaio, F. Plazaola and F. J. Teran, *Appl. Phys. Rev.*, 2015, **2**, 041302.
107 E. C. Abenojar, S. Wickramasinghe, J. Bas-Concepcion and A. C. S. Samia, *Prog. Nat. Sci.: Mater. Int.*, 2016, **26**, 440–448.
108 I. Castellanos-Rubio, I. Rodrigo, R. Munshi, O. Arriortua, J. S. Garitaonandia, A. Martinez-Amesti, F. Plazaola, I. Orue, A. Pralle and M. Insausti, *Nanoscale*, 2019, **11**, 16635–16649.
109 G. Cotin, F. Perton, C. Blanco-Andujar, B. Pichon, D. Mertz and S. Bégin-Colin, in *Nanomaterials for Magnetic and Optical Hyperthermia Applications*, Elsevier, 2018, pp. 41–60.
110 I. Conde-Leboran, D. Baldomir, C. Martinez-Boubeta, O. Chubykalo-Fesenko, M. del Puerto Morales, G. Salas, D. Cabrera, J. Camarero, F. J. Teran and D. Serantes, *J. Phys. Chem. C*, 2015, **119**, 15698–15706.
111 Z. Nemati, J. Alonso, L. M. Martinez, H. Khurshid, E. Garaio, J. A. Garcia, M.-H. H. Phan, H. Srikanth, Z. Nemati Porshokouh, J. Alonso, L. M. Martínez, H. Khurshid, E. Garaio, J. A. Garcia, M.-H. H. Phan and H. Srikanth, *J. Phys. Chem. C*, 2016, **120**, 8370–8379.
112 Z. Nemati, J. Alonso, I. Rodrigo, R. Das, E. Garaio, J. Á. García, I. Orue, M. H. Phan and H. Srikanth, *J. Phys. Chem. C*, 2018, **122**, 2367–2381.
113 R. E. E. Rosensweig, *J. Magn. Magn. Mater.*, 2002, **252**, 370–374.
114 J. P. Fortin, C. Wilhelm, J. Servais, C. Ménager, J. C. Bacri and F. Gazeau, *J. Am. Chem. Soc.*, 2007, **129**, 2628–2635.
115 N. a. Usov and B. Y. Liubimov, *J. Appl. Phys.*, 2012, **112**, 023901.
116 N. A. Usov and J. M. Barandiarán, *J. Appl. Phys.*, 2012, **112**, 053915.
117 E. C. Stoner and E. P. Wohlfarth, *Philos. Trans. R. Soc., A*, 1948, **240**, 599–642.
118 R. Chen, M. G. Christiansen and P. Anikeeva, *ACS Nano*, 2013, **7**, 8990–9000.
119 M. G. Christiansen, A. W. Senko, R. Chen, G. Romero and P. Anikeeva, *Appl. Phys. Lett.*, 2014, **104**, 213103.
120 E. Barati and M. Cinal, *Phys. Rev. B*, 2017, **95**, 134440.
121 W. T. Coffey, D. S. F. Crothers, J. L. Dormann, Y. P. Kalmykov, E. C. Kennedy and W. Wernsdorfer, *Phys. Rev. Lett.*, 1998, **80**, 5655–5658.
122 D. Gandia, L. Gandarias, L. Marcano, I. Orue, D. Gil-Cartón, J. Alonso, A. García-Arribas, A. Muela and M. L. Fdez-Gubieda, *Nanoscale*, 2020, **12**, 16081–16090.

123 H. Khurshid, P. Lampen-Kelley, Ò. Iglesias, J. Alonso, M.-H. Phan, C.-J. Sun, M.-L. Saboungi and H. Srikanth, *Sci. Rep.*, 2015, **5**, 15054.
124 M. Vasilakaki, C. Binns and K. N. Trohidou, *Nanoscale*, 2015, **7**, 7753–7762.
125 S. Ruta, R. Chantrell and O. Hovorka, *Sci. Rep.*, 2015, **5**, 1–7.
126 S. H. Noh, W. Na, J. T. Jang, J. H. Lee, E. J. Lee, S. H. Moon, Y. Lim, J. S. Shin and J. Cheon, *Nano Lett.*, 2012, **12**, 3716–3721.
127 R. P. Tan, J. Carrey and M. Respaud, *Phys. Rev. B: Condens. Matter Mater. Phys.*, 2014, **90**, 214421.
128 N. A. Usov and E. M. Gubanova, *Nanomaterials*, 2020, **10**, 1320.
129 J. Nogués, J. Sort, V. Langlais, V. Skumryev, S. Suriñach, J. S. Muñoz and M. D. Baró, *Phys. Rep.*, 2005, **422**, 65–117.
130 E. E. Fullerton, J. S. Jiang and S. D. Bader, *J. Magn. Magn. Mater.*, 1999, **200**, 392–404.
131 G. Lavorato, E. Winkler, A. Ghirri, E. Lima, D. Peddis, H. E. Troiani, D. Fiorani, E. Agostinelli, D. Rinaldi and R. D. Zysler, *Phys. Rev. B: Condens. Matter Mater. Phys.*, 2016, **94**, 054432.
132 E. Kneller and R. Hawig, *IEEE Trans. Magn.*, 1991, **27**, 3588–3600.
133 G. C. Lavorato, E. L. Winkler, E. Lima Jr and R. D. Zysler, in *Exchange Bias: From Thin Film to Nanogranular and Bulk Systems*, CRC Press, 2017, pp. 47–70.
134 I. Golosovsky, G. Salazar-Alvarez, a. López-Ortega, M. González, J. Sort, M. Estrader, S. Suriñach, M. Baró and J. Nogués, *Phys. Rev. Lett.*, 2009, **102**, 247201.
135 J. a. De Toro, D. P. Marques, P. Muñiz, V. Skumryev, J. Sort, D. Givord and J. Nogués, *Phys. Rev. Lett.*, 2015, **115**, 057201.
136 B. Shahbahrami, S. M. Rabiee and R. Shidpoor, *ACERP*, 2020, **6**, 1–15.
137 M. S. A. Darwish, H. Kim, H. Lee, C. Ryu, J. Y. Lee and J. Yoon, *Nanomaterials*, 2020, **10**, 991.
138 M. Sanna Angotzi, V. Mameli, C. Cara, A. Musinu, C. Sangregorio, D. Niznansky, H. L. Xin, J. Vejpravova and C. Cannas, *Nanoscale Adv.*, 2020, **2**, 3191–3201.
139 T. P. Almeida, F. Moro, M. W. Fay, Y. Zhu and P. D. Brown, *J. Nanopart. Res.*, 2014, **16**, 1–13.
140 J. Robles, R. Das, M. Glassell, M. H. Phan and H. Srikanth, *AIP Adv.*, 2018, **8**, 056719.
141 V. Pilati, R. Cabreira Gomes, G. Gomide, P. Coppola, F. G. Silva, F. L. O. Paula, R. Perzynski, G. F. Goya, R. Aquino and J. Depeyrot, *J. Phys. Chem. C*, 2018, **122**, 3028–3038.
142 J.-H. H. Lee, J.-T. T. Jang, J.-S. S. Choi, S. H. Moon, S.-H. H. Noh, J.-G. W. G. J.-W. J.-G. J.-W. Kim, J.-G. W. G. J.-W. J.-G. J.-W. Kim, I.-S. S. Kim, K. I. Park and J. Cheon, *Nat. Nanotechnol.*, 2011, **6**, 418–422.
143 C. Martinez-Boubeta, 2017, ArXiv:1704.08172.
144 F. Ahmad and Y. Zhou, *Chem. Res. Toxicol.*, 2017, **30**, 492–507.
145 V. Mariani, J. Ponti, G. Giudetti, F. Broggi, P. Marmorato, S. Gioria, F. Franchini, H. Rauscher and F. Rossi, *Nanotoxicology*, 2012, **6**, 272–287.
146 D. Cabrera, A. Coene, J. Leliaert, E. J. Artés-Ibáñez, L. Dupré, N. D. Telling and F. J. Teran, *ACS Nano*, 2018, **12**, 2741–2752.
147 R. Di Corato, A. Espinosa, L. Lartigue, M. Tharaud, S. Chat, T. Pellegrino, C. Ménager, F. Gazeau and C. Wilhelm, *Biomaterials*, 2014, **35**, 6400–6411.
148 T. E. Torres, E. Lima, M. P. Calatayud, B. Sanz, A. Ibarra, R. Fernández-Pacheco, A. Mayoral, C. Marquina, M. R. Ibarra and G. F. Goya, *Sci. Rep.*, 2019, **9**, 3992.
149 C. S. B. Dias, T. D. M. Hanchuk, H. Wender, W. T. Shigeyosi, J. Kobarg, A. L. Rossi, M. N. Tanaka, M. B. Cardoso and F. Garcia, *Sci. Rep.*, 2017, 1–8.
150 R. Das, C. Witanachchi, Z. Nemati, V. Kalappattil, I. Rodrigo, J. Á. García, E. Garaio, J. Alonso, V. D. Lam, A.-T. Le, M.-H. Phan and H. Srikanth, *Appl. Sci.*, 2020, **10**, 787.
151 M.-D. Yang, C.-H. Ho, S. Ruta, R. Chantrell, K. Krycka, O. Hovorka, F.-R. Chen, P.-S. Lai and C.-H. Lai, *Adv. Mater.*, 2018, **1802444**, 1802444.
152 S. K. Shaw, A. Biswas, A. Gangwar, P. Maiti, C. L. Prajapat, S. S. Meena and N. K. Prasad, *J. Magn. Magn. Mater.*, 2019, **484**, 437–444.
153 H. Khurshid, J. Alonso, Z. Nemati, M. H. Phan, P. Mukherjee, M. L. Fdez-Gubieda, J. M. Barandiarán and H. Srikanth, *J. Appl. Phys.*, 2015, **117**, 17A337.
154 G. Hemery, C. Genevois, F. Couillaud, S. Lacomme, E. Gontier, E. Ibarboure, S. Lecommandoux, E. Garanger and O. Sandre, *Mol. Syst. Des. Eng.*, 2017, **2**, 629–639.
155 V. Malik, A. Pal, O. Pravaz, J. J. Crassous, S. Granville, B. Grobety, A. M. Hirt, H. Dietsch and P. Schurtenberger, *Nanoscale*, 2017, **9**, 14405–14413.
156 P. Torruella, A. Ruiz-Caridad, M. Walls, A. G. Roca, A. López-Ortega, J. Blanco-Portals, L. López-Conesa, J. Nogués, F. Peiró and S. Estradé, *Nano Lett.*, 2018, **18**, 5854–5861.
157 M. Jiang and X. Peng, *Nano Lett.*, 2017, **17**, 3570–3575.
158 A. G. Roca, L. Gutiérrez, H. Gavilán, M. E. Fortes Brollo, S. Veintemillas-Verdaguer and M. del P. Morales, *Adv. Drug Delivery Rev.*, 2019, **138**, 68–104.
159 L. Manna, D. J. Milliron, A. Meisel, E. C. Scher and A. P. Alivisatos, *Nat. Mater.*, 2003, **2**, 382–385.
160 P. Torruella, R. Arenal, F. De La Peña, Z. Saghi, L. Yedra, A. Eljarrat, L. López-Conesa, M. Estrader, A. López-Ortega, G. Salazar-Alvarez, J. Nogués, C. Ducati, P. A. Midgley, F. Peiró and S. Estradé, *Nano Lett.*, 2016, **16**, 5068–5073.
161 G. Lavorato, E. Winkler, B. Rivas-Murias and F. Rivadulla, *Phys. Rev. B: Condens. Matter Mater. Phys.*, 2016, **94**, 054405.
162 G. C. Lavorato, E. Lima, H. E. Troiani, R. D. Zysler and E. L. Winkler, *Nanoscale*, 2017, **9**, 10240–10247.
163 A. Quesada, C. Granados-Miralles, A. López-Ortega, S. Erokhin, E. Lottini, J. Pedrosa, A. Bollero, A. M. Aragón, F. Rubio-Marcos, M. Stingaciu, G. Bertoni, C. de Julián Fernández, C. Sangregorio, J. F. Fernández, D. Berkov and M. Christensen, *Adv. Bioelectron. Mater.*, 2016, **2**, 1500365.
164 J. Lohr, A. A. de Almeida, M. S. Moreno, H. Troiani, G. F. Goya, T. E. Torres Molina, R. Fernandez-Pacheco, E. L. Winkler, M. Vasquez Mansilla, R. Cohen,

L. C. C. M. Nagamine, L. M. Rodríguez, D. E. Fregenal, R. D. Zysler and E. Lima, *J. Phys. Chem. C*, 2019, **123**, 1444–1453.

165 Z. Nedelkoski, D. Kepaptsoglou, L. Lari, T. Wen, R. A. Booth, S. D. Oberdick, P. L. Galindo, Q. M. Ramasse, R. F. L. Evans, S. Majetich and V. K. Lazarov, *Sci. Rep.*, 2017, **7**, 45997.

166 C. L. Dennis, K. L. Krycka, J. A. Borchers, R. D. Desautels, J. Van Lierop, N. F. Huls, A. J. Jackson, C. Gruettner and R. Ivkov, *Adv. Funct. Mater.*, 2015, **25**, 4300–4311.

167 A. López-Ortega, E. Lottini, G. Bertoni, C. De Julián Fernández and C. Sangregorio, *Chem. Mater.*, 2017, **29**, 1279–1289.

168 G. Lavorato, M. Alzamora, C. Contreras, G. Burlandy, F. J. Litterst and E. Baggio-Saitovitch, *Part. Part. Syst. Charact.*, 2019, **36**, 1900061.

169 E. Wetterskog, C. Tai, J. Grins, L. Bergström and G. Salazar-Alvarez, *ACS Nano*, 2013, **7**, 7132–7144.

170 B. Pacakova, S. Kubickova, G. Salas, A. R. Mantlikova, M. Marciello, M. P. Morales, D. Niznansky, J. Vejpravova, G. Salazar-Alvarez, L. Bergström, T. Brückel and J. Nogués, *Nanoscale*, 2017, **9**, 5129–5140.

171 P. Bender, J. Fock, C. Frandsen, M. F. Hansen, C. Balceris, F. Ludwig, O. Posth, E. Wetterskog, L. K. Bogart, P. Southern, W. Szczerba, L. Zeng, K. Witte, C. Grüttner, F. Westphal, D. Honecker, D. González-Alonso, L. Fernández Barquín and C. Johansson, *J. Phys. Chem. C*, 2018, **122**, 3068–3077.

172 J. M. D. Coey, *Phys. Rev. Lett.*, 1971, **27**, 1140–1142.

173 B. N. Pianciola, E. Lima, H. E. Troiani, L. C. C. M. Nagamine, R. Cohen and R. D. Zysler, *J. Magn. Magn. Mater.*, 2015, **377**, 44–51.

174 S. D. Oberdick, A. Abdelgawad, C. Moya, S. Mesbahi-Vasey, D. Kepaptsoglou, V. K. Lazarov, R. F. L. Evans, D. Meilak, E. Skoropata, J. van Lierop, I. Hunt-Isaak, H. Pan, Y. Ijiri, K. L. Krycka, J. A. Borchers and S. A. Majetich, *Sci. Rep.*, 2018, **8**, 3425.

175 Y. Ijiri, K. L. Krycka, I. Hunt-Isaak, H. Pan, J. Hsieh, J. A. Borchers, J. J. Rhyne, S. D. Oberdick, A. Abdelgawad and S. A. Majetich, *Phys. Rev. B*, 2019, **99**, 094421.

176 C. Kons, M.-H. Phan, H. Srikanth, D. A. Arena, Z. Nemati, J. A. Borchers and K. L. Krycka, *Phys. Rev. Mater.*, 2020, **4**, 034408.

177 N. Daffé, M. Sikora, M. Rovezzi, N. Bouldi, V. Gavrilov, S. Neveu, F. Choueikani, P. Ohresser, V. Dupuis, D. Taverna, A. Gloter, M.-A. Arrio, P. Sainctavit and A. Juhin, *Adv. Mater. Interfaces*, 2017, **1700599**, 1700599.

178 S. H. Moon, S. H. Noh, J. H. Lee, T. H. Shin, Y. Lim and J. Cheon, *Nano Lett.*, 2017, **17**, 800–804.

179 K. Lee, S. Lee and B. Ahn, *Chem. Mater.*, 2019, **31**, 728–736.

180 A. Ramos, J.-B. Moussy, M.-J. Guittet, M. Gautier-Soyer, C. Gatel, P. Bayle-Guillemaud, B. Warot-Fonrose and E. Snoeck, *Phys. Rev. B: Condens. Matter Mater. Phys.*, 2007, **75**, 224421.

181 L. Horng, G. Chern, M. Chen, P. Kang and D. Lee, *J. Magn. Magn. Mater.*, 2004, **270**, 389–396.

182 N. Viart, R. S. Hassan, J. L. Loison, G. Versini, F. Huber, P. Panissod, C. Mény and G. Pourroy, *J. Magn. Magn. Mater.*, 2004, **279**, 21–26.

183 J. Rodewald, J. Thien, T. Pohlmann, M. Hoppe, F. Timmer, F. Bertram, K. Kuepper and J. Wollschläger, *Phys. Rev. B*, 2019, **100**, 155418.

184 M. S. Carrião and A. F. Bakuzis, *Nanoscale*, 2016, **8**, 8363–8377.

185 A. Chiu-Lam and C. Rinaldi, *Adv. Funct. Mater.*, 2016, **26**, 3933–3941.

186 A. Riedinger, P. Guardia, A. Curcio, M. A. Garcia, R. Cingolani, L. Manna and T. Pellegrino, *Nano Lett.*, 2013, **13**, 2399–2406.

187 H. C. Davis, S. Kang, J. H. Lee, T. H. Shin, H. Putterman, J. Cheon and M. G. Shapiro, *Biophys. J.*, 2020, **118**, 1502–1510.

188 R. Piñol, C. D. S. Brites, R. Bustamante, A. Martínez, N. J. O. Silva, J. L. Murillo, R. Cases, J. Carrey, C. Estepa, C. Sosa, F. Palacio, L. D. Carlos and A. Millán, *ACS Nano*, 2015, **9**, 3134–3142.

189 G. Lavorato, E. Lima, M. Vasquez Mansilla, H. Troiani, R. Zysler and E. Winkler, *J. Phys. Chem. C*, 2018, **122**, 3047–3057.

190 F. Lin and J. I. Zink, *J. Am. Chem. Soc.*, 2020, **142**, 5212–5220.

191 N. S. Abadeer and C. J. Murphy, *J. Phys. Chem. C*, 2016, **120**, 4691–4716.

192 Z. Li, A. Aranda-Ramos, P. Güell-Grau, J. L. Tajada, L. Pou-Macayo, S. Lope Piedrafita, F. Pi, A. G. Roca, M. D. Baró, J. Sort, C. Nogués, J. Nogués and B. Sepúlveda, *Appl. Mater. Today*, 2018, **12**, 430–440.

193 A. Espinosa, M. Bugnet, G. Radtke, S. Neveu, G. A. Botton, C. Wilhelm and A. Abou-Hassan, *Nanoscale*, 2015, **7**, 18872–18877.

194 Z. Zhou, Y. Sun, J. Shen, J. Wei, C. Yu, B. Kong, W. Liu, H. Yang, S. Yang and W. Wang, *Biomaterials*, 2014, **35**, 7470–7478.

195 A. Espinosa, R. Di Corato, J. Kolosnjaj-Tabi, P. Flaud, T. Pellegrino and C. Wilhelm, *ACS Nano*, 2016, **10**, 2436–2446.

196 Z. Li, J. Jin, F. Yang, N. Song and Y. Yin, *Nat. Commun.*, 2020, **11**, 1–11.

197 L. León Félix, B. Sanz, V. Sebastián, T. E. Torres, M. H. Sousa, J. A. H. Coaquira, M. R. Ibarra and G. F. Goya, *Sci. Rep.*, 2019, **9**, 4185.

198 M. V. Efremova, V. A. Naumenko, M. Spasova, A. S. Garanina, M. A. Abakumov, A. D. Blokhina, P. A. Melnikov, A. O. Prelovskaya, M. Heidelmann, Z.-A. Li, Z. Ma, I. V. Shchetinin, Y. I. Golovin, I. I. Kireev, A. G. Savchenko, V. P. Chekhonin, N. L. Klyachko, M. Farle, A. G. Majouga and U. Wiedwald, *Sci. Rep.*, 2018, **8**, 11295.

199 A. Moser, K. Takano, D. T. Margulies, M. Albrecht, Y. Sonobe, Y. Ikeda, S. Sun and E. E. Fullerton, *J. Phys. D: Appl. Phys.*, 2002, **35**, R157–R167.

200 H. Zeng, J. Li, J. Liu, Z. Wang and S. Sun, *Nature*, 2002, **420**, 395–398.

201 D. Robert, D. Fayol, C. Le Visage, G. Frasca, S. Brulé, C. Ménager, F. Gazeau, D. Letourneur and C. Wilhelm, *Biomaterials*, 2010, **31**, 1586–1595.
202 C. Blanco-Andujar, A. Walter, G. Cotin, C. Bordeianu, D. Mertz, D. Felder-Flesch and S. Begin-Colin, *Nanomedicine*, 2016, **11**, 1889–1910.
203 P. L. McCormack, *Drugs*, 2012, **72**, 2013–2022.
204 I. M. Obaidat, B. Issa and Y. Haik, *Nanomaterials*, 2014, **5**, 63–89.
205 Y. Zhang, W. Zhang, C. Geng, T. Lin, X. Wang, L. Zhao and J. Tang, *Prog. Nat. Sci.*, 2009, **19**, 1699–1704.
206 H. Gerad, D. A. Van Echo, M. Whitacre, M. Ashman, M. Helrich, J. Foy, S. Ostrow, P. H. Wiernik and J. Aisner, *Cancer*, 1984, **53**, 2585–2591.
207 M. Unni, A. M. Uhl, S. Savliwala, B. H. Savitzky, R. Dhavalikar, N. Garraud, D. P. Arnold, L. F. Kourkoutis, J. S. Andrew and C. Rinaldi, *ACS Nano*, 2017, **11**, 2284–2303.
208 R. Chen, M. G. Christiansen, A. Sourakov, A. Mohr, Y. Matsumoto, S. Okada, A. Jasanoff and P. Anikeeva, *Nano Lett.*, 2016, **16**, 1345–1351.
209 S. Tong, C. A. Quinto, L. Zhang, P. Mohindra and G. Bao, *ACS Nano*, 2017, **11**, 6808–6816.
210 R. Hergt, R. Hiergeist, M. Zeisberger, D. Schüler, U. Heyen, I. Hilger and W. A. Kaiser, *J. Magn. Magn. Mater.*, 2005, **293**, 80–86.
211 W. Liu, L. Chen, M. Chen, W. Wang, X. Li, H. Yang, S. Yang and Z. Zhou, *Adv. Healthcare Mater.*, 2020, 2000202.
212 F. Perton, M. Tasso, G. A. Muñoz Medina, M. Ménard, C. Blanco-Andujar, E. Portiansky, M. B. F. van Raap, D. Bégin, F. Meyer, S. Begin-Colin and D. Mertz, *Appl. Mater. Today*, 2019, **16**, 301–314.
213 M. Abdulla-Al-Mamun, Y. Kusumoto, T. Zannat, Y. Horie and H. Manaka, *RSC Adv.*, 2013, **3**, 7816.
214 H.-W. Yang, H.-L. Liu, M.-L. Li, I.-W. Hsi, C.-T. Fan, C.-Y. Huang, Y.-J. Lu, M.-Y. Hua, H.-Y. Chou, J.-W. Liaw, C.-C. M. Ma and K.-C. Wei, *Biomaterials*, 2013, **34**, 5651–5660.
215 L. Huang, L. Ao, D. Hu, W. Wang, Z. Sheng and W. Su, *Chem. Mater.*, 2016, **28**, 5896–5904.
216 J. Keyvan Rad, Z. Alinejad, S. Khoei and A. R. Mahdavian, *ACS Biomater. Sci. Eng.*, 2019, **5**, 4425–4434.
217 Z. Fan, M. Shelton, A. K. Singh, D. Senapati, S. A. Khan and P. C. Ray, *ACS Nano*, 2012, **6**, 1065–1073.
218 Q. Lu, X. Dai, P. Zhang, X. Tan, Y. Zhong, C. Yao, M. Song, G. Song, Z. Zhang, G. Peng, Z. Guo, Y. Ge, K. Zhang and Y. Li, *Int. J. Nanomed.*, 2018, **13**, 2491–2505.
219 L. M. Sanchez and V. A. Alvarez, *Bioengineering*, 2019, **6**, 75.
220 J. Zhu, Y. Lu, Y. Li, J. Jiang, L. Cheng, Z. Liu, L. Guo, Y. Pan and H. Gu, *Nanoscale*, 2014, **6**, 199–202.
221 H. Y. Zhao, S. Liu, J. He, C. C. Pan, H. Li, Z. Y. Zhou, Y. Ding, D. Huo and Y. Hu, *Biomaterials*, 2015, **51**, 194–207.
222 J. Li, L. Zheng, H. Cai, W. Sun, M. Shen, G. Zhang and X. Shi, *ACS Appl. Mater. Interfaces*, 2013, **5**, 10357–10366.
223 H. Lee, T.-J. Yoon and R. Weissleder, *Angew. Chem.*, 2009, **121**, 5767–5770.
224 T. J. Yoon, H. Lee, H. Shao, S. A. Hilderbrand and R. Weissleder, *Adv. Mater.*, 2011, **23**, 4793–4797.
225 S. Cheong, P. Ferguson, K. W. Feindel, I. F. Hermans, P. T. Callaghan, C. Meyer, A. Slocombe, C.-H. Su, F.-Y. Cheng, C.-S. Yeh, B. Ingham, M. F. Toney and R. D. Tilley, *Angew. Chem.*, 2011, **123**, 4292–4295.
226 Z. Zhou, L. Yang, J. Gao and X. Chen, *Adv. Mater.*, 2019, **31**, 1–32.
227 F. A. Cardona, E. S. Urquiza, P. de la Presa, S. H. Tobón, U. Pal, P. H. Fraijo, M. J. Yacaman, J. D. Lozada Ramírez, R. Ivkov, A. Angulo-Molina and M. Á. Méndez-Rojas, *RSC Adv.*, 2016, **6**, 77558–77568.
228 Z. Zhou, R. Bai, J. Munasinghe, Z. Shen, L. Nie and X. Chen, *ACS Nano*, 2017, **11**, 5227–5232.
229 F. Li, D. Zhi, Y. Luo, J. Zhang, X. Nan, Y. Zhang, W. Zhou, B. Qiu, L. Wen and G. Liang, *Nanoscale*, 2016, **8**, 12826–12833.
230 G. H. Im, S. M. Kim, D.-G. Lee, W. J. Lee, J. H. Lee and I. S. Lee, *Biomaterials*, 2013, **34**, 2069–2076.
231 M. Yamaguchi, A. Ito, A. Ono, Y. Kawabe and M. Kamihira, *ACS Synth. Biol.*, 2014, **3**, 273–279.
232 R. Chen, G. Romero, M. G. Christiansen, A. Mohr and P. Anikeeva, *Science*, 2015, **347**(80), 1477–1480.
233 I. Orue, L. Marcano, P. Bender, A. García-Prieto, S. Valencia, M. A. Mawass, D. Gil-Cartón, D. Alba Venero, D. Honecker, A. García-Arribas, L. Fernández Barquín, A. Muela and M. L. Fdez-Gubieda, *Nanoscale*, 2018, **10**, 7407–7419.
234 L. M. Lacroix, N. Frey Huls, D. Ho, X. Sun, K. Cheng and S. Sun, *Nano Lett.*, 2011, **11**, 1641–1645.
235 S. Liébana-Viñas, K. Simeonidis, U. Wiedwald, Z.-A. Li, Z. Ma, E. Myrovali, A. Makridis, D. Sakellari, G. Vourlias, M. Spasova, M. Farle and M. Angelakeris, *RSC Adv.*, 2016, **6**, 72918–72925.
236 M. R. Phadatare, J. V Meshram, K. V Gurav, J. H. Kim and S. H. Pawar, *J. Phys. D: Appl. Phys.*, 2016, **49**, 095004.
237 M. Angelakeris, Z.-A. Li, M. Hilgendorff, K. Simeonidis, D. Sakellari, M. Filippousi, H. Tian, G. Van Tendeloo, M. Spasova, M. Acet and M. Farle, *J. Magn. Magn. Mater.*, 2015, **381**, 179–187.